Evaluation of EC-CCM for numerical simulation of diesel-ignited ammonia combustion

Yulong Liu

15th June 2026

ISSN: 0282-1990
ISRN: LUTMDN/TMHP-26/5693-SE

Abstract

The maritime sector needs to reduce greenhouse gas emissions and improve the sustainability of energy systems. Ammonia has attracted increasing attention as a potential carbon-free marine fuel. However, ammonia has low reactivity, a high ignition energy requirement, and a low flame propagation speed, which make stable combustion difficult. Diesel-ignited ammonia combustion is therefore a promising method for improving ammonia combustion performance.

This work is based on previous experimental studies conducted in a constant-volume combustion chamber under high-pressure and high-temperature conditions, as well as on a lab-scale, water-cooled two-stroke engine at Dalian University of Technology. In the engine experiments, liquid ammonia and diesel were directly injected into the cylinder through two opposing injectors. This provided relevant conditions for studying diesel–ammonia dual-fuel combustion.

In this thesis, numerical simulations were carried out using OpenFOAM. The aim was to investigate how injection angle and injector position affect flame development, ignition, combustion intensity, and pollutant formation. Three different injection configurations were compared under similar operating conditions.

The results show that the injection strategy has a significant influence on the combustion process. Case 1 showed the most stable late-stage combustion. Case 2 produced the highest heat release rate and the strongest localized combustion intensity. Case 3 showed earlier ignition but weaker stability during the later combustion stage. Differences in the distributions of NO and N_2O also indicate that the interaction between the diesel and ammonia jets affects the formation of nitrogen-containing pollutants.

To reduce computational cost, Chemistry Coordinate Mapping (CCM) and Error-Controlled Chemistry Coordinate Mapping (EC-CCM) were used. Both methods reduced the computational time. EC-CCM provided the best balance between accuracy and efficiency. Compared with the standard chemistry solver, EC-CCM achieved an acceleration of approximately 3.67×, while maintaining good agreement in pressure, temperature, and OH results.

This study provides numerical insight into diesel–ammonia dual-fuel combustion under high-pressure conditions and shows that EC-CCM is a promising method for accelerating detailed CFD simulations of combustion.

Keywords: OpenFOAM, diesel–ammonia combustion, marine engine, EC-CCM, pollutant emissions

Sammanfattning

Sjöfartssektorn behöver minska utsläppen av växthusgaser och förbättra energisystemens hållbarhet. Ammoniak har fått ökad uppmärksamhet som ett potentiellt kolfritt marint bränsle. Ammoniak har dock låg reaktivitet, högt tändenergibehov och låg flamhastighet, vilket gör stabil förbränning svår. Dieselantänd ammoniak-förbränning är därför en lovande metod för att förbättra ammoniakens förbrännings-prestanda.

Detta arbete bygger på tidigare experimentella studier i en konstantvolym-förbrännings-kammare vid högt tryck och hög temperatur, samt på en laboratoriebaserad, vattenkyld tvåtaktsmotor vid Dalian University of Technology. I motorexperimenten injicerades flytande ammoniak och diesel direkt i cylindern genom två motstående injektorer. Detta gav relevanta förhållanden för studier av diesel–ammoniak tvåbränsle-förbränning.

I detta examensarbete genomfördes numeriska simuleringar med OpenFOAM. Syftet var att undersöka hur insprutnings-vinkel och injektorposition påverkar flamutveckling, tändning, förbrännings-intensitet och förorenings-bildning. Tre olika insprutnings-konfigurationer jämfördes under liknande driftförhållanden.

Resultaten visar att insprutnings-strategin har stor betydelse för förbränningen. Fall 1 gav den mest stabila sena förbränningen. Fall 2 hade den högsta värmeavgivningen och den starkaste lokala förbrännings-intensiteten. Fall 3 visade tidigare tändning men svagare stabilitet i det senare förbrännings-skedet. Skillnader i NO- och N_2O-fördelning visar också att samspelet mellan diesel- och ammoniakstrålarna påverkar bildningen av kvävehaltiga föroreningar.

För att minska beräknings-kostnaden användes Chemistry Coordinate Mapping (CCM) och Error-Controlled Chemistry Coordinate Mapping (EC-CCM). Båda metoderna minskade beräkningstiden. EC-CCM gav den bästa balansen mellan noggrannhet och effektivitet. Jämfört med standardkemilösaren uppnådde EC-CCM en acceleration på cirka 3.67×, samtidigt som god överensstämmelse bibehölls för tryck, temperatur och OH.

Denna studie ger numerisk insikt i diesel–ammoniak tvåbränsle-förbränning under högtrycks-förhållanden och visar att EC-CCM är en lovande metod för att påskynda detaljerade CFD-simuleringar av förbränning.

Nyckelord: OpenFOAM; diesel–ammoniak-förbränning; marin motor; EC-CCM; förorenings-utsläpp

Acknowledgements

I would like to express my sincere gratitude to my supervisor, Professor Xue-Song Bai, for his guidance, support, and valuable advice throughout this thesis work. His expertise and suggestions have been very helpful in the development of this study.

I would also like to thank my examiner, Professor Hesameddin Fatehi, for his time, evaluation, and valuable comments on this thesis.

I am also grateful to Yuchen Zhou, Margherita Miccio, and Zichen Qiu for their assistance and support during the numerical simulation work. Their previous studies, suggestions, and discussions helped me better understand diesel–ammonia dual-fuel combustion, OpenFOAM simulations, and chemistry acceleration methods.

Special thanks are given to Lund University and the Division of Combustion Engines for providing the academic environment and computational resources required for this research. I am also grateful for the support from the LUMI high-performance computing platform, which made the large-scale simulations possible.

Finally, I would like to thank my family and friends for their continuous encouragement, patience, and support during my master's study.

Popular Science Summary

Ships usually use diesel or other fossil fuels. These fuels are easy to burn and can produce strong power. However, they also produce carbon dioxide and other harmful emissions. Carbon dioxide is one of the main gases that cause global warming and sea level rise. Therefore, future marine engines need cleaner fuels to reduce their impact on the environment.

Ammonia is one possible clean fuel. It does not contain carbon, so it does not directly produce carbon dioxide when it burns. However, ammonia is difficult to use in engines. It is hard to ignite, burns slowly, and its flame is not very stable. Because of this, ammonia usually needs another fuel to help it burn. In this thesis, diesel is used as the ignition fuel. Diesel burns first and creates a hot region. Then ammonia can burn in this hot region.

This thesis studies diesel–ammonia combustion for future marine engines. The main aim is to understand how the positions and angles of the diesel and ammonia injectors affect the combustion process. In simple words, this study looks at how diesel and ammonia meet inside the combustion chamber, and how this changes the flame, heat release, and pollutant emissions.

This study uses computer simulations in OpenFOAM. The simulation conditions are based on high-pressure and high-temperature engine-like conditions. Three different injection arrangements are compared. In addition, a chemistry acceleration method called EC–CCM is tested. This is because the standard simulation method takes a long time. The aim is to see whether EC–CCM can make the simulation faster while still keeping the main results reliable.

Three injection strategies/cases are studied. The results show that the injection arrangement has a strong effect on diesel–ammonia combustion. In Case 1, the ammonia jet partly bypasses the main hot region created by the diesel. Therefore, the ammonia reaction is not strong; the ammonia remains largely unburned.

In Case 2, ammonia interacts more strongly with the hot products from diesel combustion. This gives the highest heat release rate and strong local combustion. However, the ammonia jet also tends to dilute and quench the hot region, so the reaction becomes weaker in the later stage.

In Case 3, diesel and ammonia meet more directly in an opposing-jet arrangement. This helps ammonia react more strongly. However, it also makes the combustion more intense and increases pollutant formation.

For emissions, NO is mainly formed in high-temperature combustion regions. Therefore, stronger ammonia combustion may produce more NO. N_2O and unburned NH_3 are more related to incomplete ammonia combustion and lower-temperature regions. This

means that lower NO emissions do not always mean better ammonia combustion.

The results show that ammonia needs good contact with the hot region created by the diesel to burn well. If this contact is weak, ammonia burns poorly. If the interaction is too strong, the combustion process and emissions may become harder to control.

Finally, EC–CCM makes the simulation about 3.67 times faster than the standard chemistry solver. At the same time, the main pressure, temperature, and OH results are still close to the standard method.

Overall, this thesis shows that ammonia can be a useful fuel for future marine engines, but its combustion must be carefully controlled. A good injection design needs to balance stable combustion, good ammonia use, and low pollutant emissions.

Notations and Symbols

Latin letters

A_0	Nozzle outlet area
A_d	Droplet surface area
B_M	Spalding mass transfer number
C_d	Discharge coefficient
C_e	SGS model constant
C_k	SGS viscosity model constant
C_{KH}	Kelvin–Helmholtz breakup constant
$c_{p,d}$	Droplet specific heat capacity
d	Droplet diameter
d_m	Characteristic droplet diameter
D_k	Diffusion coefficient of species k
D_v	Vapor diffusion coefficient
$F(d)$	Droplet size cumulative distribution function
F_D	Drag force
F_g	Gravitational force
f_i	Body force in the i-direction
h	Convective heat transfer coefficient
h_{vap}	Latent heat of vaporization
i, j	Spatial direction indices
$J^{SGS} * k, i$	SGS diffusion flux of species k
k	Species index
$k * sgs$	SGS turbulent kinetic energy
k_g	Gas thermal conductivity
m_d	Droplet mass

$\dot{m} * evap$	Evaporation rate
$\dot{m} * inj$	Injection mass flow rate
$nSlice$	Number of slices in EC–CCM
Nu	Nusselt number
p	Pressure
Pr	Prandtl number
q	Rosin–Rammler distribution parameter
$\dot{Q} * conv$	Convective heat transfer rate
R	Gas constant
Re_d	Droplet Reynolds number
S_m	Mass source term
$S * Y_k$	Species source term
$\widetilde{S} * ij$	Filtered strain-rate tensor
t	Time
$t * KH$	Kelvin–Helmholtz breakup time
T	Temperature
T_d	Droplet temperature
T_g	Gas temperature
u_i	Gas velocity component
u_d	Droplet velocity
u_{inj}	Injection velocity
x_i	Spatial coordinate
x_d	Droplet position
Y_k	Mass fraction of species k

X

Greek letters

α	Diesel injection angle
β	Ammonia injection angle
γ	Spray cone angle
Δ	LES filter size
ΔP	Injection pressure difference
Δu	Gas–liquid relative velocity
δ_{ij}	Kronecker delta
μ	Dynamic viscosity
μ_{sgs}	SGS viscosity
ρ	Gas density
ρ_f	Fuel density
ρ_g	Gas-phase density
ρ_l	Liquid density
σ_{ij}	Viscous stress tensor
σ_k	SGS model constant
$\tau^{sgs} * ij$	SGS stress tensor
$\tau * ij$	Stress tensor
ϕ	General scalar variable
$\dot{\omega}_k$	Chemical reaction rate of species k

Contents

1 Introduction

1.1 Background

The excessive emission of greenhouse gases has led to an increase in global average temperature and sea level. Therefore, reducing greenhouse gas emissions and achieving net-zero carbon emissions is of great significance. In absolute terms, carbon dioxide, the main gas causing the greenhouse effect, accounts for roughly 16.2% of total Greenhouse Gas (GHG) emissions, and the transport sector accounts for about 23% of global energy-related CO_2 emissions, as shown in Figure 1.1. The carbon emissions from the propulsion systems of transportation vehicles account for about 70% of direct transport emissions, and reducing these emissions will greatly accelerate the process of achieving net-zero carbon emissions.

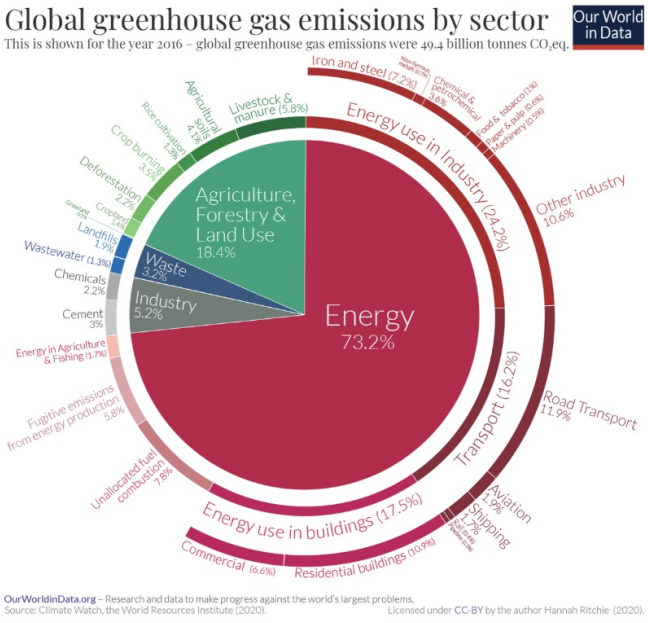

Figure 1.1: Global greenhouse gas emissions by sector [1].

In addition to carbon emissions, the power system of transportation also generates CO, NO_x, HC, SO_2, $PM_{2.5}$, which pose a risk to human health if inhaled excessively. Moreover, traditional power systems use fossil fuels; with the long-term and large-scale use of fossil fuels, the issue of fossil fuel reserves is also a concern. For the future development of the Earth and the healthy life of humanity, reforming power systems that use traditional fuels is of great significance.

The fundamental energy source for typical propulsion systems in transportation is fossil fuel combustion. Fossil fuels consist primarily of carbon-based materials, hydrocarbons, and their derivatives [2]. When combusted, they generate a preponderance of heat. This heat is converted into mechanical driving power by the propulsion system. During this

part of the process, fossil fuels undergo combustion and breakdown, which generates a saturation of smaller carbon-based gases. Under complete oxidation conditions, the main combustion product of fossil fuels is carbon dioxide (CO_2). This leads to the inevitable emission of carbon dioxide and other greenhouse gases in propulsion systems that rely on fossil fuels as their core energy source. In view of this, green fuels have become the focus of current research due to their extremely low or even zero greenhouse gas emissions during combustion.

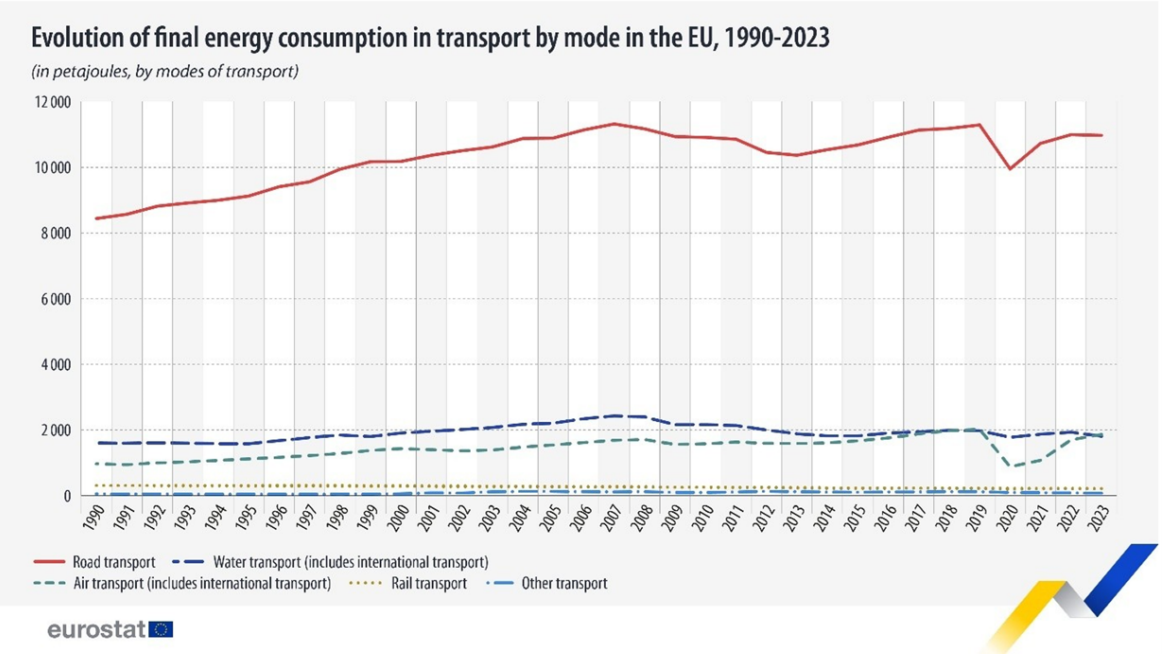

Figure 1.2: Evolution of final energy consumption in different transport sectors in the EU, highlighting the role of water transport, 1990–2023 [3].

Figure 1.2 shows the evolution of energy consumption in water transport in the EU from 1990 to 2023 [3]. Water transport has maintained relatively high energy consumption over the past decades, underscoring its important role in international trade and freight transportation. Therefore, improving the energy efficiency and reducing emissions of marine transportation are important for the sustainable development of the shipping industry.

In recent years, the International Maritime Organization (IMO) has proposed increasingly strict decarbonization targets for international shipping. The 2023 IMO GHG Strategy aims to reduce total greenhouse gas emissions from international shipping by at least 20% by 2030, striving for 30%, and by at least 70% by 2040, striving for 80%, compared with 2008 levels, with the long-term target of achieving net-zero emissions by or around 2050 [4].

To achieve these emission reduction targets, improving the combustion efficiency of marine engines and promoting the application of clean energy have become increasingly important. Therefore, research on advanced marine engine combustion technologies and clean energy has attracted growing attention in recent years. In this Master's thesis, Everllence two-stroke diesel engines are taken as the research object to investigate the combustion processes occurring inside the engine and to compare the combustion

characteristics of conventional fossil fuels and green fuels.

Everllence two-stroke diesel engines can operate on natural gas using a dual-fuel combustion concept. In this concept, natural gas is directly injected into the cylinder at a high pressure of around 300 bar, while ignition is initiated by a small amount of pilot diesel fuel. This combustion mode enables gaseous fuels to be used in large two-stroke engines while maintaining relatively stable ignition and combustion control.

To study the main processes involved in such combustion systems, optical experiments have recently been carried out at Dalian University of Technology (DUT) using a constant volume combustion chamber. The experiments are designed to represent key features of dual-fuel operation in internal combustion engines. The controlled chamber conditions make these processes easier to observe and analyze.

Based on the experiments at DUT and previous simulation studies conducted within the research group, this thesis focuses on the numerical investigation of diesel-ignited ammonia combustion using OpenFOAM. The work mainly investigates the interaction between high-pressure fuel injection, pilot diesel ignition, and ammonia combustion under high-temperature and high-pressure conditions. In addition, the error-controlled chemistry coordinate mapping (EC-CCM) method is applied to improve the computational efficiency of detailed combustion chemistry simulations.

1.2 Literature review

1.2.1 Diesel-ignited ammonia engines

Companies such as Everllence, which are involved in heavy-duty propulsion systems, particularly in the maritime sector, are currently focusing on developing low-carbon or even carbon-free shipping solutions. As a result, green hydrogen, ammonia, methanol, biofuels, and other alternative fuels have been taken into consideration as potential energy sources for future marine propulsion systems [5].

In recent years, numerous studies have evaluated the potential of different alternative fuels for marine applications. For instance, a recent review published in Nature Energy compared several marine fuel candidates, including hydrogen, ammonia, methane, and methanol. The study concluded that ammonia represents the most balanced carbon-free fuel option, while methanol is considered the most balanced carbon-containing alternative fuel [6]. In addition, Kanchiralla et al. [7] evaluated the technological feasibility, environmental impact, and economic viability of different energy carriers for three types of vessels, namely a RoPax ferry, a tanker, and a service vessel. The investigated energy carriers included battery-electric systems and three electrofuels (hydrogen, methanol, and ammonia), which were combined with both internal combustion engines and fuel cells. Their study showed that ammonia fuel resulted in the lowest life-cycle cost among the three reference vessels.

Ammonia is an ideal alternative fuel for the maritime sector, and the most significant challenge in using ammonia as a marine fuel lies in engine combustion technology. To

overcome ammonia's inherent shortcoming of high ignition energy, narrow flammability limit, and slow propagation speed [8], various pilot-diesel-ignition ammonia combustion modes have received widespread attention, including increasing spark energy, supercharging the engine, and introducing a second fuel [9]. Among these methods, a dual-fuel premixed combustion approach, known as the Reactivity Controlled Compression Ignition (RCCI) concept, provides a feasible solution for ammonia engines. This concept, proposed by Reitz et al., aims to boost engine thermal efficiency while reducing NO and soot emissions in compression-ignition engines [9]. RCCI concept involves introducing two fuels with different reactivity into the cylinder. A low-reactivity fuel is injected to form a homogeneous mixture, while a high-reactivity fuel, such as diesel or biodiesel, ignites the fuel/air mixture [9].

At present, many studies have investigated the relationship between injection timing and fuel reactivity. Yousefi et al. [10] investigated that diesel injection timing strongly affects the ignition and combustion processes in RCCI combustion by altering spray-air mixing, ignition kernel formation, and local reaction conditions. Advanced injection generally improves fuel-air mixing and combustion completeness, while excessively early injection may prolong ignition delay due to lower in-cylinder temperature. In contrast, retarded injection tends to reduce the available mixing time, which may deteriorate combustion efficiency and increase incomplete combustion emissions such as unburned NH_3 and soot.

Zhou et al. [11] performed direct numerical simulation (DNS) of diesel/ammonia RCCI combustion and found multiple combustion modes taking place: ignition, premixed flame propagation, and diffusion combustion. NO and N_2O emissions are governed by the interaction of different combustion modes.

Another approach, using Ammonia-Diesel Dual-Fuel (ADDF) diffusion combustion, in which liquid ammonia and liquid diesel are directly injected into a compression-ignition engine, has also proven a feasible strategy for burning ammonia. Since the two fuels are injected directly, there is flexibility in controlling their mixing to optimize combustion efficiency and reduce pollutant emissions.

The direct injection of liquid ammonia into ICEs faces several technical challenges, such as unclear flash boiling mechanisms and the need for specially designed injection systems. Bjørgen et al. investigated the combustion modes and pollutant emissions of ammonia/diesel dual-fuel combustion under three different ammonia energy shares and various injection timings. The experimental results showed that ammonia injection timing significantly affects the combustion process. Early ammonia injection tends to produce premixed-type combustion, but it can lead to incomplete combustion, increased ammonia slip, and higher N_2O emissions. When ammonia is injected shortly before diesel injection, the vaporization cooling effect of liquid ammonia prolongs the ignition delay. In contrast, temporal overlap between ammonia and diesel injections can improve combustion efficiency and reduce ammonia slip and N_2O emissions, although it also leads to increased NOx emissions [12].

In addition to injection timing, the spatial interaction between ammonia and diesel sprays also affects combustion development and emission formation. Xu et al. [13] investigated the effects of ammonia/diesel spray interaction on combustion and emissions

under engine-relevant conditions. The results showed that ammonia mixes faster than diesel under evaporating conditions, and the timing of spray interaction plays an important role in ammonia combustion. Early interaction promotes ammonia ignition by the diesel flame and helps sustain combustion, whereas late interaction leads to a leaner and colder ammonia/air mixture, resulting in unstable combustion or even flame extinction. In addition, N_2O is mainly formed in the quenching region of the ammonia flame, indicating that optimizing ammonia/diesel injection strategies is important for improving combustion efficiency and reducing N_2O emissions.

Furthermore, Xu et al. [14] extended the investigation to practical engine conditions. They conducted an experimental and numerical study on the combustion and emission characteristics of a two-stroke, low-speed, direct-injection compression-ignition ammonia/diesel dual-fuel engine under different ammonia energy ratios. The results showed that increasing ammonia substitution significantly reduced conventional pollutant emissions, with NOx emissions decreasing by up to approximately 42% and CO emissions decreasing by about 80–92%. However, the addition of ammonia significantly increased N_2O emissions by more than two orders of magnitude, leading to a substantial increase in total greenhouse gas emissions.

1.2.2 CFD simulation of dual-fuel combustion

CFD simulations have been widely applied in combustion and spray studies because they can provide detailed information about flow fields, fuel-air mixing, ignition, flame propagation, and emissions formation inside combustion systems. Compared with experimental methods, CFD simulations allow the transient combustion process to be analyzed in greater detail under controlled conditions. In addition, modern CFD tools include various turbulence, spray, evaporation, and combustion models that are suitable for high-pressure dual-fuel combustion simulations. Their parallel computing capability also makes large-scale simulations with detailed chemical reactions possible.

Chu et al. [15] employ the three-dimensional numerical simulation software CONVERGE 3.0 to conduct numerical simulations of the effects of ammonia energy ratio and hydrogen addition on the performance of ammonia-diesel dual-fuel engine. Xu et al. [9] utilized an in-house solver developed on the OpenFOAM V7 platform to show that ammonia-diesel dual-fuel combustion can significantly reduce greenhouse gas emissions in marine engines, but challenges such as high NH_3 slip, NO_x, and N_2O emissions remain due to the low reactivity and slow flame propagation of ammonia.

Since CFD simulations of diesel–ammonia engines require capturing multi-mode combustion [11], detailed transport models and chemical kinetics must be coupled with the flow field. A major challenge is the high computational cost associated with integrating chemical reaction mechanisms, which typically involve hundreds of species and reactions. Several novel approaches have been proposed to accelerate the integration of chemical reaction rates; a comprehensive review is provided in Ref. [16]. One such approach is chemistry coordinate mapping (CCM) [17], which has been successfully applied in multiple ammonia engine simulations [9, 13, 14]. More recently, Zhou et al. [18] extended this method by incorporating error control and automated selection of CCM control variables. However, the error-controlled CCM (EC-CCM) approach has not yet

been validated for ADDF combustion engines.

1.3 Knowledge gap and research goals

In this thesis, OpenFOAM will be used to perform numerical simulations of the combustion chamber. The key tasks include establishing the combustion chamber model, defining the combustion conditions, analyzing the combustion results, and applying the EC-CCM method to improve the computational efficiency of the simulation process.

This thesis focuses on the diesel–ammonia dual-fuel direct-injection compression-ignition combustion system. The effects of fuel injection angle and injection position on the combustion characteristics will be investigated under different operating conditions. In addition, the acceleration capability and computational performance of the EC-CCM algorithm will be evaluated and compared with the original CCM and standard chemistry approaches.

Based on the literature review, the identified knowledge gaps can be summarized as follows:

- Limited understanding of the interaction between high-pressure ammonia injection and pilot diesel ignition in diesel–ammonia dual-fuel combustion.
- Insufficient investigation of the effects of fuel injection strategies, including injection direction and injection position, on the combustion characteristics of diesel–ammonia systems.
- Challenges remain in accurately simulating diesel–ammonia dual-fuel combustion processes in the constant volume combustion chamber using OpenFOAM.
- Further investigation is still required regarding the application of the EC-CCM method to improve the computational efficiency of diesel–ammonia combustion simulations.

The research goals of this thesis can be divided into the following parts:

- To investigate the influence of fuel injection position and angle on the combustion characteristics under experimental diesel–ammonia dual-fuel combustion conditions.
- To evaluate the impact of the EC-CCM algorithm on the computational performance of the combustion simulations.

2 Methodology

This thesis employs large eddy simulation (LES) to investigate the interaction between ammonia and diesel flames, with a focus on turbulence, spray dynamics, and combustion processes. The simulations were conducted using the computational fluid dynamics (CFD) software OpenFOAM-V7 [19] and an in-house solver developed by Xu et al. [13]. This solver was specifically designed to handle two independent injectors for different fuels.

The original OpenFOAM software was mainly configured for spray simulations involving a single fuel component. Xu et al. [13] adopted an Eulerian–Lagrangian approach to model the fluid dynamics of the spray combustion process. In this framework, the gas phase was treated from the Eulerian perspective using an LES turbulence model, while the liquid phase was described using the Lagrangian method, thereby improving computational efficiency.

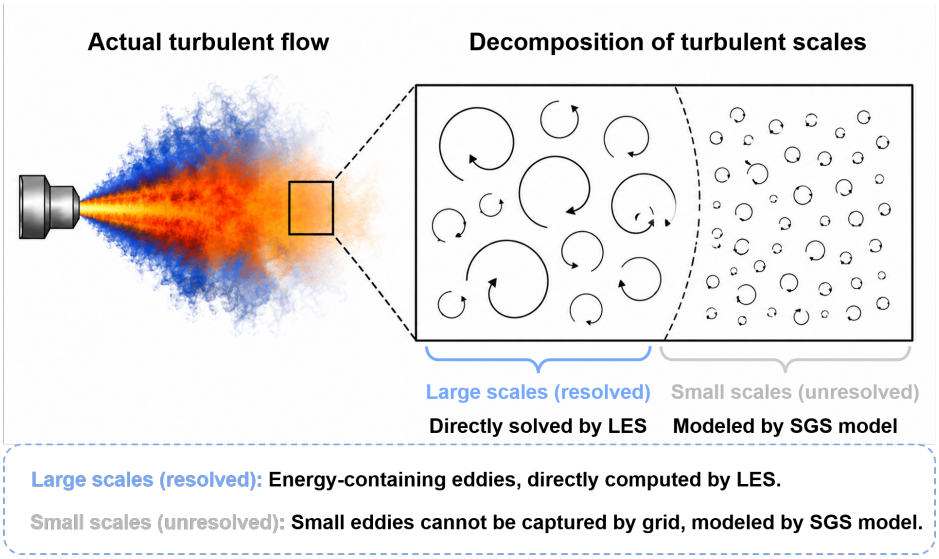

Figure 2.1: Turbulence and LES/SGS Decomposition Diagram.

In LES, large-scale turbulent structures are directly resolved, while the smaller unresolved turbulent motions are modeled using the sub-grid scale (SGS) model. Since the computational mesh cannot capture all turbulent scales, the SGS model is applied in the gas phase to account for the effects of unresolved turbulence on momentum, energy, and species transport (as shown in Figure 2.1). In this study, the one-equation eddy SGS model was adopted.

The initial droplet size distribution was modeled using the Rosin–Rammler distribution function. To improve computational efficiency, the injected fuel was represented by parcels with different initial diameters. The initial droplet velocity and injection rate were determined based on the high-pressure common-rail injection model proposed by Xu et al. [20]. As illustrated in Figure 2.2, aerodynamic instabilities during spray

development lead to secondary droplet breakup, which was modeled using the KH-RT breakup model. Heat exchange between droplets and the surrounding gas phase was described by the Ranz–Marshall heat transfer model, while droplet evaporation was calculated using the Spalding evaporation model. The interaction between the evaporated fuel vapor and turbulent gas flow was resolved using the LES-SGS turbulence model [20].

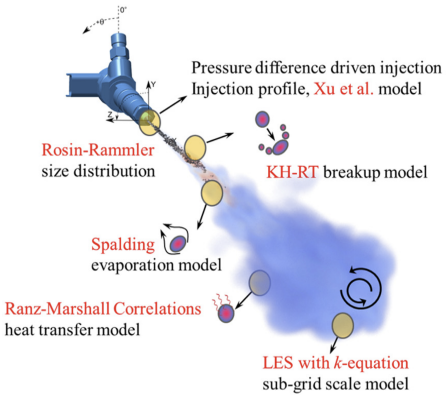

Figure 2.2: Numerical framework and sub-models used in the spray combustion simulation [20].

2.1 Governing equations

2.1.1 Gas-Phase Governing Equations

For the gas phase, which can be regarded as a continuous medium, the Eulerian approach is employed for numerical solution. In the diesel–ammonia dual-fuel combustion process, the governing equations of the gas phase mainly include the continuity equation, momentum equation, energy equation, and species transport equation. These equations are derived from the law of mass, momentum, and energy conservation and are coupled with the LES method to account for turbulent effects.

Continuity Equation

During the spray combustion process, liquid fuel droplets continuously evaporate and release vapor into the gas phase. Therefore, a source term S_m is introduced into the continuity equation to represent the mass exchange between the liquid and gas phases.

For closed CVCC, gas density changes significantly in space and time due to combustion heat release and fuel evaporation. Therefore, the continuity equation is solved in a compressible form.

The continuity equation is used to describe the conservation of mass in the gas phase:

$$\frac{\partial \rho}{\partial t} + \frac{\partial (\rho u_i)}{\partial x_i} = S_m \tag{2.1}$$

where: ρ is the gas density; u_i is the velocity component in the x_i-direction; S_m is the mass source term caused by droplet evaporation.

Momentum Equation

The filtered momentum equation employed in the present LES framework was derived from the compressible Navier–Stokes equations using Favre spatial filtering. The SGS stress was modeled using the one-equation eddy viscosity model implemented in OpenFOAM and adopted in previous studies [19, 20, 21].

$$\frac{\partial(\bar{\rho}\tilde{u}_i)}{\partial t} + \frac{\partial(\bar{\rho}\tilde{u}_i\tilde{u}_j)}{\partial x_j} = -\frac{\partial \bar{p}}{\partial x_i} + \frac{\partial \bar{\sigma}_{ij}}{\partial x_j} - \frac{\partial \tau_{ij}^{sgs}}{\partial x_j} + \bar{\rho}\tilde{f}_i \tag{2.2}$$

where τ_{ij}^{sgs} represents the SGS stress:

$$\tau_{ij}^{sgs} = \bar{\rho}\left(\widetilde{u_i u_j} - \tilde{u}_i\tilde{u}_j\right) \tag{2.3}$$

$\tilde{f}_i$ is the momentum source term resulting from the injected liquid fuel sprays.

Unlike the Reynolds-averaged Navier–Stokes (RANS) turbulence model, LES applies spatial filtering to the Navier–Stokes equations. Favre density-weighted filtering for any physical quantity ϕ is defined as:

$$\tilde{\phi} = \frac{\overline{\rho\phi}}{\bar{\rho}} \tag{2.4}$$

Since LES can only directly resolve large-scale turbulent structures, the small-scale turbulence is modeled using the SGS model. In this study, the one-equation eddy SGS model is adopted to simulate sub-grid scale turbulent effects.

The SGS stress tensor is modeled as:

$$\tau_{ij}^{sgs} = -2\mu_{sgs}\left(\tilde{S}_{ij} - \frac{1}{3}\tilde{S}_{kk}\delta_{ij}\right) + \frac{1}{3}\tau_{kk}^{sgs}\delta_{ij} \tag{2.5}$$

where the SGS viscosity is calculated by:

$$\mu_{sgs} = C_k\bar{\rho}k_{sgs}^{1/2}\Delta \tag{2.6}$$

and the strain-rate tensor is defined as:

$$\tilde{S}_{ij} = \frac{1}{2}\left(\frac{\partial\tilde{u}_i}{\partial x_j} + \frac{\partial\tilde{u}_j}{\partial x_i}\right) \tag{2.7}$$

where: Δ is the LES filter size; k_{sgs} is the SGS turbulent kinetic energy.

During spray combustion, high-pressure injection generates strong jet flows, shear layers, and turbulent mixing. Therefore, the momentum equation plays an important role in predicting flame propagation, spray penetration, and fuel–air mixing.

SGS Turbulent Kinetic Energy Equation

The transport equation for SGS turbulent kinetic energy is expressed as [20]:

$$\frac{\partial(\bar{\rho}k_{sgs})}{\partial t} + \frac{\partial(\bar{\rho}\tilde{u}_j k_{sgs})}{\partial x_j} = -\tau_{ij}\frac{\partial \tilde{u}_i}{\partial x_j} - C_e\frac{\bar{\rho}k_{sgs}^{3/2}}{\Delta} + \frac{\partial}{\partial x_j}\left[\left(\mu + \frac{\mu_{sgs}}{\sigma_k}\right)\frac{\partial k_{sgs}}{\partial x_j}\right] \tag{2.8}$$

where the model constants are set as: $C_k = 0.05$, $C_e = 0.05$, $\sigma_k = 0.05$

Species Transport Equation

The transport equation for each chemical species is expressed as:

$$\frac{\partial(\rho Y_k)}{\partial t} + \frac{\partial(\rho u_i Y_k)}{\partial x_i} = \frac{\partial}{\partial x_i}\left(\rho D_k \frac{\partial Y_k}{\partial x_i}\right) - \frac{\partial J_{k,i}^{SGS}}{\partial x_i} + \dot{\omega}_k + S_{Y_k} \tag{2.9}$$

where: Y_k is the mass fraction of species k; D_k is the diffusion coefficient; $J_{k,i}^{SGS}$ is the SGS diffusion flux; $\dot{\omega}_k$ is the chemical reaction rate; S_{Y_k} is the source term caused by droplet evaporation.

The number of species considered in this study is 69 based on the chemical kinetic mechanism of Xu et al. [22], including NH_3, n-heptane, O_2, OH, and major combustion products. In particular, the OH radical is used to identify the high-temperature reaction zone and characterize the ignition and flame propagation processes during dual-fuel combustion.

Equation of State

The ideal gas equation of state is employed to close the governing equations:

$$p = \rho R T \sum \frac{Y_i}{W_i} \tag{2.10}$$

where: R is the universal gas constant; T is the temperature, W_i is the molecular weight of species i.

2.1.2 Liquid-Phase Governing Equations

After being injected from the injector, the liquid fuel undergoes primary atomization, secondary breakup, heat transfer, evaporation, and interaction with the turbulent gas phase. The governing equations for these processes are described as follows.

Injection Model

The injection process was modeled using the pressure-driven common-rail injection model proposed by Xu et al. [23]. The injection velocity is calculated as:

$$u_{inj} = \sqrt{\frac{2\Delta P}{\rho_f}} \tag{2.11}$$

The injection mass flow rate is given by:

$$\dot{m}_{inj} = C_d A_0 \rho_f u_{inj} \tag{2.12}$$

where u_{inj} is the injection velocity, ΔP is the pressure difference between the injector and combustion chamber, ρ_f is the fuel density, $\dot{m}_{inj}$ is the injection mass flow rate, C_d is the discharge coefficient, and A_0 is the nozzle outlet area.

Droplet Size Distribution

The initial droplet diameter distribution was described using the Rosin–Rammler distribution function:

$$F(d) = 1 - \exp\left[-\left(\frac{d}{d_m}\right)^q\right] \tag{2.13}$$

where $F(d)$ is the cumulative distribution function for droplets smaller than diameter d, d_m is the characteristic diameter, and q is the distribution parameter.

Secondary Breakup Model

The secondary breakup of droplets was modeled using the KH-RT breakup model. The characteristic breakup time of Kelvin–Helmholtz instability is expressed as:

$$t_{KH} = C_{KH} \frac{d}{\sqrt{\rho_g/\rho_l}\,|\Delta u|} \tag{2.14}$$

where d is the droplet diameter, ρ_g and ρ_l are the gas and liquid densities, respectively, $|\Delta u|$ is the relative velocity between gas and liquid phases, and C_{KH} is an empirical constant.

Heat Transfer Model

The convective heat transfer between droplets and surrounding gas is calculated using the Ranz–Marshall correlation:

$$\dot{Q}_{conv} = hA_d(T_g - T_d) \tag{2.15}$$

$$h = \frac{Nu\, k_g}{d} \tag{2.16}$$

$$Nu = 2 + 0.6Re_d^{1/2}Pr^{1/3} \tag{2.17}$$

where A_d is the droplet surface area, T_g and T_d are the gas and droplet temperatures, k_g is the gas thermal conductivity, Re_d is the droplet Reynolds number, and Pr is the Prandtl number.

Evaporation Model

The droplet evaporation rate is expressed as:

$$\frac{dm_d}{dt} = -\dot{m}_{evap} \tag{2.18}$$

$$\dot{m}_{evap} = \frac{A_d \rho_g D_v}{d} \ln(1 + B_M) \tag{2.19}$$

where ρ_g is the gas density, D_v is the vapor diffusion coefficient, and B_M is the Spalding mass transfer number.

Droplet Motion Equation

The droplet motion is described using the Lagrangian approach:

$$\frac{d\mathbf{x}_d}{dt} = \mathbf{u}_d \tag{2.20}$$

$$m_d \frac{d\mathbf{u}_d}{dt} = \mathbf{F}_D + \mathbf{F}_g \tag{2.21}$$

where $\mathbf{x}_d$ and $\mathbf{u}_d$ are the droplet position and velocity, respectively, $\mathbf{F}_D$ is the drag force, and $\mathbf{F}_g$ is the gravitational force.

Droplet Energy Equation

The droplet temperature evolution is governed by:

$$m_d c_{p,d} \frac{dT_d}{dt} = \dot{Q}_{conv} - \dot{m}_{evap} h_{vap} \tag{2.22}$$

where $c_{p,d}$ is the droplet specific heat capacity and h_{vap} is the latent heat of vaporization.

2.2 CFD solver

The numerical simulations were performed using OpenFOAM-v7 [19] with the DDFSsprayFoam solver developed by Xu et al. [13]. This solver was developed for dual-fuel spray combustion and allows two independent injectors to be used for different fuels.

The solver is based on the finite volume method within an Eulerian–Lagrangian framework. The compressible reacting gas phase was solved in the Eulerian field using the PIMPLE algorithm, while the liquid fuel sprays were represented by Lagrangian parcels. The coupling between the gas and liquid phases was considered through source terms of mass, momentum, energy, and species. LES was employed to resolve the large-scale turbulent structures, while the unresolved turbulence was modeled using a sub-grid scale model. Detailed chemical kinetics of Xu et al. [22], which consists of 69 species and 389 reactions, were coupled with the combustion process, and the CCM method [17, 16] was applied to accelerate the chemistry calculation.

2.3 Boundary conditions

The computational domain was initialized according to the experimental CVCC conditions. The initial pressure and temperature inside the chamber were set to 5.63 MPa and 830 K, respectively. The initial gas velocity was initialized as a stationary field.

For the chamber walls, no-slip boundary conditions were applied to the velocity field:

$$\mathbf{U} = 0 \tag{2.23}$$

Zero-gradient boundary conditions were applied to pressure, temperature, and species mass fractions at the wall boundaries:

$$\frac{\partial p}{\partial n} = 0 \tag{2.24}$$

$$\frac{\partial T}{\partial n} = 0 \tag{2.25}$$

$$\frac{\partial Y_k}{\partial n} = 0 \tag{2.26}$$

Wall functions were employed for turbulence-related quantities, including turbulent kinetic energy, turbulent viscosity, and turbulent thermal diffusivity.

2.4 CCM acceleration method

The traditional Standard chemistry method directly solves the detailed chemical reaction equations in every CFD cell at each time step. Since the governing equations for continuity, momentum, energy, and species are solved separately in a segregated and iterative manner, the computational cost of chemical source term evaluation becomes particularly expensive in combustion simulations involving detailed chemistry [17].

Zhou's study, based on a three-dimensional combustion simulation of ammonia/n-heptane reactivity controlled compression ignition (RCCI) using 6400 CPU cores, showed that the evaluation of chemical reaction source terms dominated the computational cost of the simulation process, accounting for approximately 88% of the total simulation time, as illustrated in Figure 2.3. In comparison, the pressure and species transport equations accounted for only about 5% each, while the remaining equations collectively occupied less than 2% of the total computational time [16, 18]. This demonstrates that chemistry calculations are the major computational bottleneck in detailed combustion simulations, thereby motivating the use of chemistry acceleration methods such as CCM and EC-CCM to improve computational efficiency.

Unlike the traditional Standard chemistry method, where detailed chemical reactions are solved independently in every CFD cell, CCM maps the physical domain into a low-dimensional phase space constructed using several thermodynamic variables as independent variables. Cells with similar thermochemical states are grouped into the same phase-space zone, where chemistry integration is performed only once, and the resulting reaction rates are subsequently mapped back to the corresponding physical cells [17, 24]. Since multiple CFD cells can share a single chemistry calculation, the number of ODE chemistry integrations can be significantly reduced, thereby improving computational efficiency. Compared with full direct numerical simulation (DNS) calculations, the CCM approach was able to maintain good prediction accuracy while reducing computational cost by more than 70% [17].

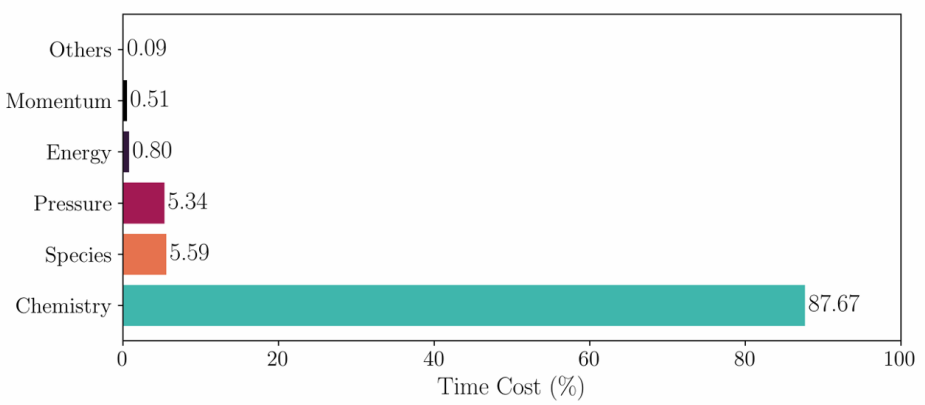

Figure 2.3: Breakdown of computational time across simulation stages [16].

To further improve the robustness and prediction accuracy of the CCM approach, the EC-CCM method was subsequently developed [16, 18]. Compared with the original CCM method, EC-CCM introduces adaptive error control and dynamic variable selection through the ecVars system, which allows important thermochemical variables to be selected automatically during the simulation process. Important species variables can be dynamically added or removed according to their contribution to the evolution of the combustion state, thereby improving the adaptability of the mapping procedure. The adaptive criterion is controlled through a tolerance associated with the number of slices,

$$\text{Tolerance} = \frac{1}{nSlice}$$

which enables dynamic optimization of the mapping variables during the simulation. As a result, EC-CCM improves both the mapping accuracy and the stability of combustion prediction, particularly during the ignition and transient combustion stages. In addition, EC-CCM incorporates optimized parallel communication and timing analysis functions, further improving computational efficiency in large-scale parallel simulations.

3 Experimental rig and CFD cases

3.1 Experimental rig

The experiments were carried out in a constant-volume combustion chamber (CVCC) equipped with four large track-shaped optical windows, each measuring 220 mm × 90 mm. Diesel and ammonia injectors were installed on opposite sides of the chamber, while the remaining two windows were used for optical diagnostics. As illustrated in Fig. 3.1, the system includes dual-fuel injection units along with devices for controlling the ambient temperature and pressure inside the CVCC.

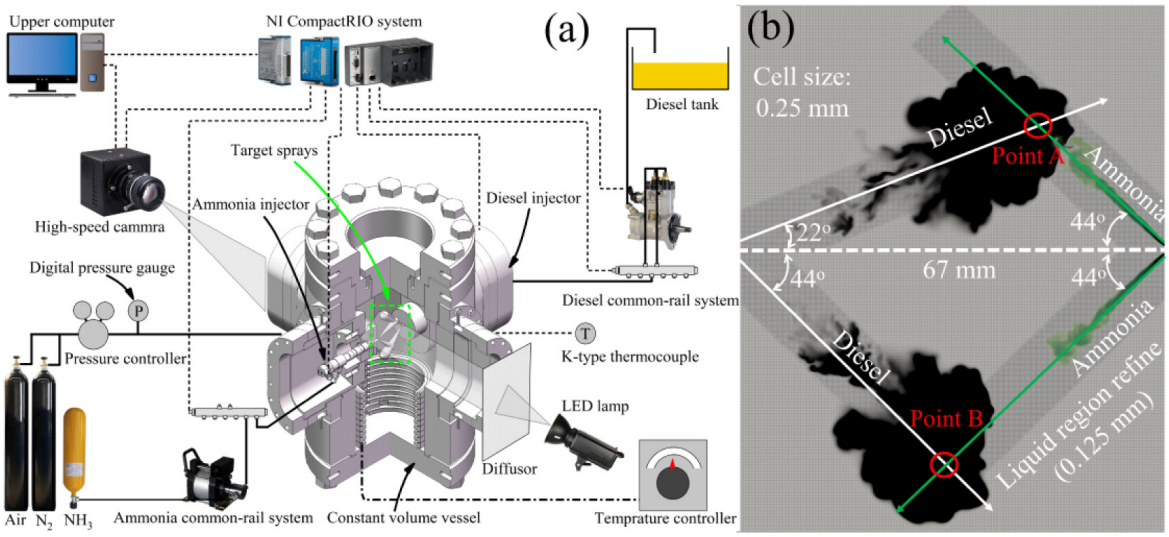

Figure 3.1: (a) high-pressure and high-temperature CVCC [25, 13].

Both diesel and ammonia are supplied through electronically controlled common-rail injection systems. Diesel pressure is generated by an electronic pump, whereas ammonia pressure is maintained using a gas–liquid booster pump. The injectors are housed in mounts with internal water cooling, maintaining temperatures above 80 °C. The chamber pressure is regulated by a pressure reducer with an accuracy of ±100 kPa. Heating is provided by an electrical heating wire located at the bottom of the vessel, with a maximum power output of 12 kW controlled via a voltage regulator. Temperature is monitored using K-type thermocouples with a precision of ±10 K. The heating elements are positioned at the base of the vessel, while temperature measurements are taken along the plane of the injector axes.

Spray and combustion processes are visualized using Diffused Back-Illumination (DBI) and natural flame luminosity imaging techniques. In the DBI method, an adjustable LED light source is employed to capture both evaporating and non-evaporating sprays. A polytetrafluoroethylene (PTFE) plate is placed in front of the light source to act as a diffuser, producing uniform illumination. The light passes through the spray and is recorded by a high-speed camera. For combustion imaging, the natural flame luminosity

method is used by eliminating background illumination and sealing the corresponding optical window, allowing direct recording of flame emissions. Diesel flames emit intense radiation mainly due to soot incandescence, resulting in bright luminosity, whereas ammonia flames are dominated by chemiluminescence from reactive radicals and appear much dimmer with an orange-yellow color.

A high-speed color camera (FASTCAM Mini UX5) operating at 10,000 frames per second with an exposure time of 1/128000 s is used to capture ignition and flame development in detail. The experimental system is controlled using a CompactRIO platform, with control software developed in LabVIEW. This setup enables precise synchronization between fuel injection and image acquisition. Further details regarding the experimental setup, including equipment specifications and measurement uncertainties, can be found in Ref. [25].

3.2 Operating conditions

3.2.1 Initial Chamber Conditions

Table 3.1: Initial chamber conditions used in the simulation.

Parameter	Value
Ambient gas composition	Air
O_2 mass fraction	0.22
N_2 mass fraction	0.78
Initial chamber pressure	5.63 MPa
Initial chamber temperature	830 K

The combustion chamber was initially filled with air composed of O_2 and N_2 with mass fractions of 0.22 and 0.78, respectively. The initial chamber pressure and temperature were set to 5.63 MPa and 830 K, respectively.

3.2.2 Fuel Injection Conditions

Table 3.2: Fuel injection conditions used in the simulation.

Parameter	Diesel	Ammonia
Fuel species	$C_{12}H_{26}$	NH_3
Injection model	Cone injection	Cone injection
Start of injection (ms)	0	1.2
Injection duration (ms)	0.79434	2.017
Injection pressure (MPa)	78	68
Nozzle diameter (mm)	0.170	0.240
Injected mass (mg)	3.37	18.17
Spray cone angle (°)	8.0	7.0

The fuel injection conditions used in the present simulations are summarized in Table 3.2. Diesel fuel, represented by $C_{12}H_{26}$ for physical properties and C_7H_{16} for chemical properties, was employed as the pilot fuel, while ammonia was used as the main injected fuel. Both fuels were introduced into the combustion chamber using the cone injection model.

Diesel injection started at 0 ms with an injection duration of 0.79434 ms, whereas ammonia injection was initiated at 1.2 ms and lasted for 2.017 ms. The injection pressures for diesel and ammonia were set to 78 MPa and 68 MPa, respectively. The nozzle diameters were specified as 0.170 mm for diesel and 0.240 mm for ammonia. In addition, the total injected fuel masses were 3.37 mg for diesel and 18.17 mg for ammonia. The spray cone angles were fixed at 8° for diesel and 7° for ammonia, respectively, in order to represent the spray dispersion characteristics under high-pressure injection conditions.

3.2.3 Numerical Setup

Mesh generation

The computational mesh was generated using OpenFOAM meshing utilities blockMesh, snappyHexMesh, and refineMesh. A structured hexahedral background mesh was first created using blockMesh. The computational domain was defined as a rectangular chamber with dimensions of $80 \times 120 \times 120$ mm^3, and the initial background mesh consisted of $20 \times 30 \times 30$ cells.

Local mesh refinement was applied in the fuel injection and combustion regions using snappyHexMesh. Additional cylindrical refinement regions were arranged along the diesel and ammonia spray directions with a radius of 5 mm and refinement level 4. The mesh generation process included castellated mesh generation and snapping. Mesh quality was controlled by limiting the maximum non-orthogonality to 65 and the maximum internal skewness to 4. Finally, the checkMesh utility was used to verify the mesh quality before the simulations. The mesh was decided based on the work of Xu et al. [13]. A coarser mesh than that of Xu et al. [13] was used, and it was shown that similar combustion characteristics were obtained.

Solver and turbulence model

The simulations were performed using the OpenFOAM-based reacting spray solver DDFSSprayFoam. The solver was used for transient compressible reacting flows with Lagrangian spray tracking and detailed chemical reactions. Turbulence effects were modeled using the Large eddy simulation approach with the one-equation k-SGS model as discussed in the previous section. The simulations were conducted under transient conditions with coupled spray, evaporation, and combustion processes.

Spray and breakup models

A Lagrangian discrete parcel approach was used to simulate the liquid fuel sprays, and both diesel and ammonia injections were described using the coneInjection model. Droplet evaporation was modeled using the liquidEvaporationBoil model, while droplet breakup was described using the Reitz KH–RT model (ReitzKHRT). Spray dispersion was modeled using the stochastic dispersion LES model, and droplet-wall interaction was treated using rebound boundary conditions.

Chemistry model

Detailed chemical kinetics of Xu et al. [22] were used to simulate the dual-fuel combustion process. Chemical source terms were solved using the ordinary differential equation (ODE) chemistry solver implemented in OpenFOAM. To improve computational efficiency, the CCM method [17] was applied for chemistry acceleration. Both the original CCM algorithm and EC-CCM approach [16, 18] were investigated and compared in this work.

Numerical schemes

A transient finite volume method was adopted for all governing equations. First-order Euler discretization was used for temporal integration. Cell-centered interpolation was applied for thermodynamic quantities, while the velocity field employed the cellPoint interpolation scheme. The maximum Courant number was limited to 0.1 to ensure numerical stability during the transient spray combustion simulations.

Parallel computation

The simulations were performed on the LUMI high-performance computing (HPC) platform using parallel computation. Domain decomposition was carried out using the decomposePar utility in OpenFOAM. The computational cases were executed in parallel using up to 400 CPU cores through the SLURM workload manager. After the simulations, the results were reconstructed using the reconstructPar utility for post-processing and visualization.

3.3 Case setup

The operating conditions and injection configurations for the three simulation cases are summarized in Table 3.3. In all cases, diesel was used as the pilot fuel, and Ammonia was used as the main fuel injected. Diesel injection timing and pressure were fixed at 0 ms and 78 MPa, respectively, while Ammonia injection timing and pressure were

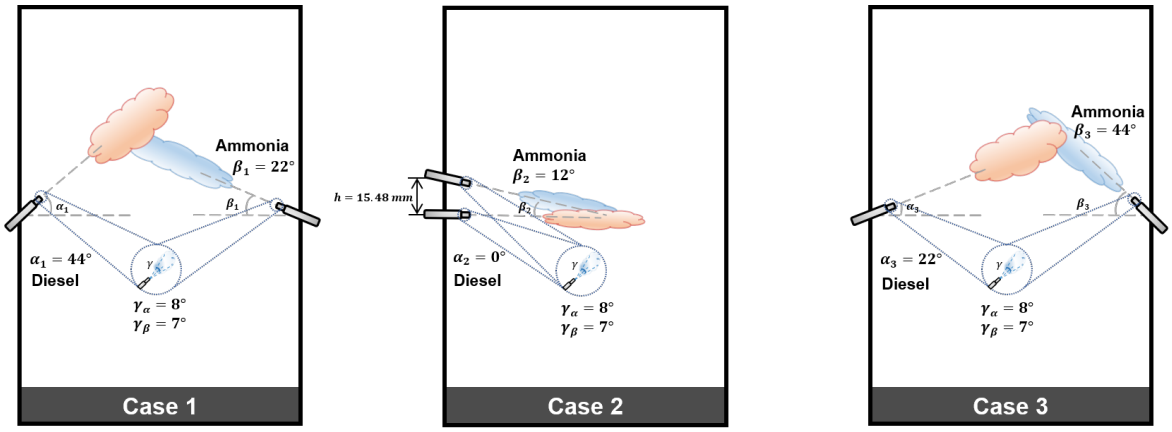

Figure 3.2: Schematic diagrams of Cases 1–3.

maintained at 1.2 ms and 68 MPa. The diameters of the nozzles for the diesel and Ammonia injections were kept constant at 0.170 mm and 0.240 mm, respectively.

The schematic diagrams for the three simulation cases are shown in Figure 3.2. The main differences among the three cases were the injector arrangement and injection directions. Case 1 used an opposing-jet configuration, where the diesel and Ammonia jets were directed upward at 44° and 22°, respectively. Case 2 adopted a parallel-jet configuration, in which the diesel jet was injected horizontally while the Ammonia jet was directed downward at 12°, with the Ammonia injector positioned 15.84 mm above the diesel injector. Case 3 also used an opposing-jet configuration, but the injection angles were modified to 22° upward for diesel and 44° upward for Ammonia. These configurations were designed to investigate the influence of injector arrangement and jet interaction on the spray development and combustion characteristics of the diesel–ammonia dual-fuel system.

Table 3.3: Injection and operating conditions for different simulation cases.

Items	Case 1	Case 2	Case 3
Configuration	Opposing jets	Parallel jets	Opposing jets
Diesel injection angle	44° upward	0° horizontal	22° upward
NH_3 injection angle	22° upward	12° downward	44° upward
NH_3 injector position	Right side	15.84 mm above diesel injector	Right side
Diesel:			
Injection timing (ms)		0	
Injection pressure (MPa)		78	
Nozzle diameter (mm)		0.170	
Ammonia:			
Injection timing (ms)		1.2	
Injection pressure (MPa)		68	
Nozzle diameter (mm)		0.240	

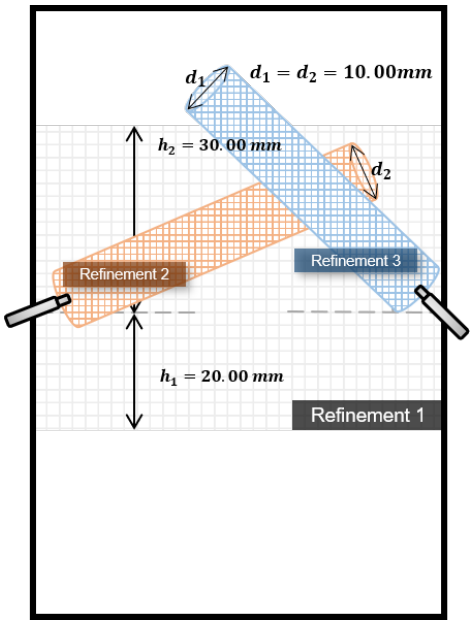

Figure 3.3: Schematic illustration of the computational mesh and refinement regions.

3.4 Computational Mesh and Local Refinement

The computational mesh was generated using the blockMesh, refineMesh, and snappyHexMesh utilities in OpenFOAM. A structured background mesh was first created to cover the entire constant-volume combustion chamber. The computational domain size was $80 \times 120 \times 120\,\mathrm{mm}^3$, and the initial background mesh was discretized into $20 \times 30 \times 30$ structured hexahedral cells. During the mesh refinement process, a hexahedral-dominant topology was maintained as much as possible in order to improve numerical stability and reduce discretization errors. In addition, mesh refinement was applied simultaneously in all three spatial directions to ensure relatively uniform spatial resolution in the key reacting regions.

As illustrated in Figure 3.3, three local refinement regions were applied. Refinement 1 was defined as a large rectangular refinement box covering the main combustion region to provide sufficient overall spatial resolution. Furthermore, two cylindrical refinement regions were introduced along the spray paths to improve the resolution of spray breakup, evaporation, ignition kernel formation, fuel-air mixing, and flame propagation processes. Refinement 2 and Refinement 3 corresponded to the main fuel spray and diesel pilot spray paths, respectively. Their directions were adaptively adjusted according to the injection orientations in different simulation cases to ensure that the high-resolution refinement regions accurately covered the actual spray development zones.

In the original mesh configuration, the rectangular refinement region and cylindrical spray-path refinement regions were refined to level 4 and level 5, respectively. However, the resulting mesh contained approximately 20 million cells, leading to excessive computational cost and simulation time for large-scale LES calculations. Therefore, in the present study, the overall refinement level was uniformly reduced by one level to balance computational accuracy and computational efficiency. Consequently, the rectangular refinement region was refined to level 3, while the cylindrical spray-path

refinement regions were refined to level 4. Both cylindrical refinement regions had a radius of 5 mm. The vertical distances between the injector locations and the chamber centerline were defined as $h_1 = 20\,\text{mm}$ and $h_2 = 30\,\text{mm}$, respectively. In addition, the parameter nCellsBetweenLevels was set to 2 to ensure smooth mesh transition between adjacent refinement levels and maintain good mesh quality.

4 Results and discussion

4.1 Grid independence study

A grid independence study was conducted for Case 1 using a coarse mesh and a fine mesh with 284,588 and 2,151,124 cells, respectively. Both meshes passed the OpenFOAM checkMesh procedure without failed mesh checks. The mesh quality parameters are listed in Table 4.1.

Table 4.1: Mesh quality parameters.

Parameter	Coarse Mesh	Fine Mesh
Cells	284,588	2,151,124
Max non-orthogonality	25.2394	25.2394
Average non-orthogonality	5.1854	3.83161
Skewness	0.333333	0.333333
Aspect ratio	1	1

Figure 4.1 compares the pressure histories obtained using the two meshes. The results show very similar pressure trends and peak values. The peak pressures predicted by the coarse and fine meshes were 5.667229 MPa and 5.666369 MPa, respectively, with a difference of approximately 0.015%. The maximum temperatures predicted by the coarse and fine meshes were 2598.806 K and 2617.216 K, respectively, corresponding to a difference of approximately 0.7%.

These small differences indicate that the numerical results are not significantly affected by further mesh refinement. Therefore, the fine mesh was selected for subsequent simulations.

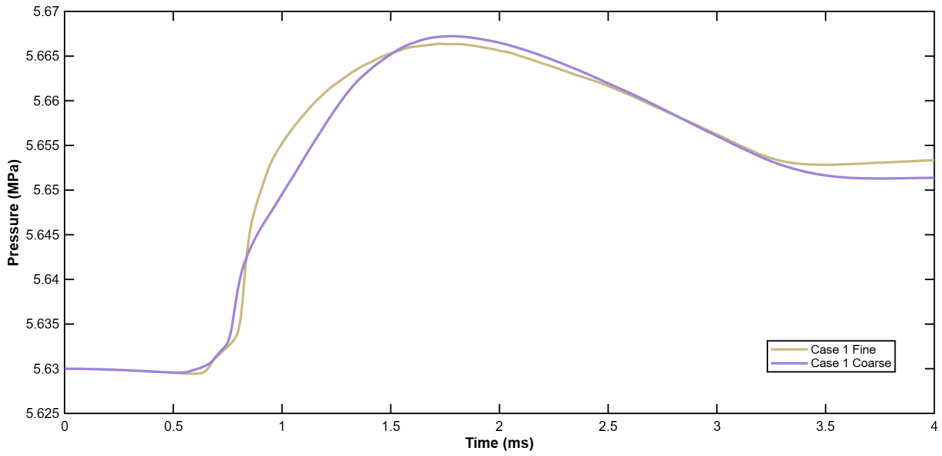

Figure 4.1: Comparison of pressure histories between the coarse and fine meshes.

4.2 Validation with experiments

To verify the accuracy and reliability of the simulation results, the numerical results obtained in this study were compared with the experimental and simulation results reported by Xu et al. [13], with particular emphasis on the comparison of temperature distribution contours at different time instants (as shown in Figure 4.2). The combustion evolution process, including ignition timing, flame propagation direction, and high-temperature region development, was used as the reference for validation in the present study.

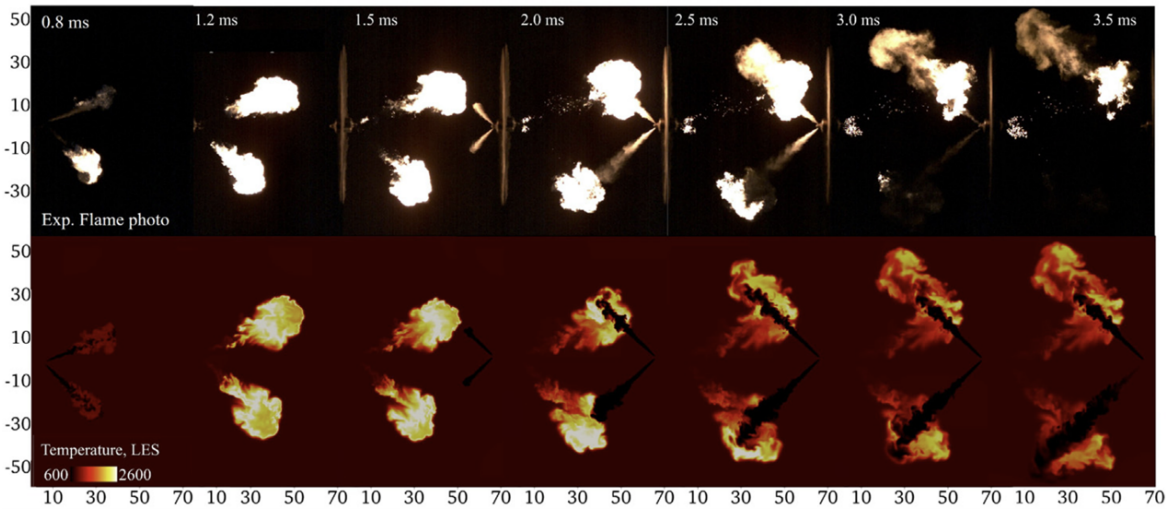

Figure 4.2: Comparison of experimental flame images and LES temperature distributions reported by Xu et al. at different time instants [13].

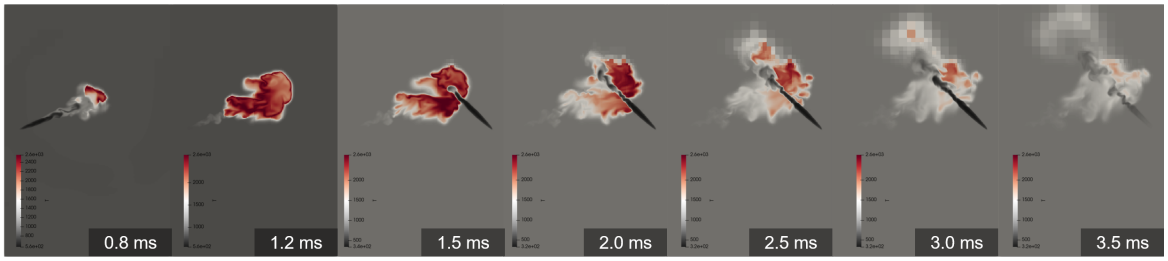

Figure 4.3: Temperature distributions at different times from the present simulation.

The validation results obtained in this work showed generally good qualitative agreement with both the experimental observations and the reference LES results (as shown in Figures 4.2 and 4.3). In particular, the main flame structures, ignition locations, and overall combustion development trends at different time instants were reasonably captured. The simulated high-temperature regions also exhibited similar spatial distributions and propagation characteristics compared with the reference results.

However, some discrepancies remained in the detailed flame morphology and late-stage turbulent structures, where the present simulation produced relatively smoother flame boundaries and less fragmented structures. These differences may be related to mesh resolution, turbulence modelling, spray sub-models, and the difference between temperature contours and experimental flame luminosity images. Overall, the comparison

indicates that the present numerical setup is capable of reliably predicting the major combustion characteristics of the dual-fuel spray combustion process.

4.3 Combustion process analysis

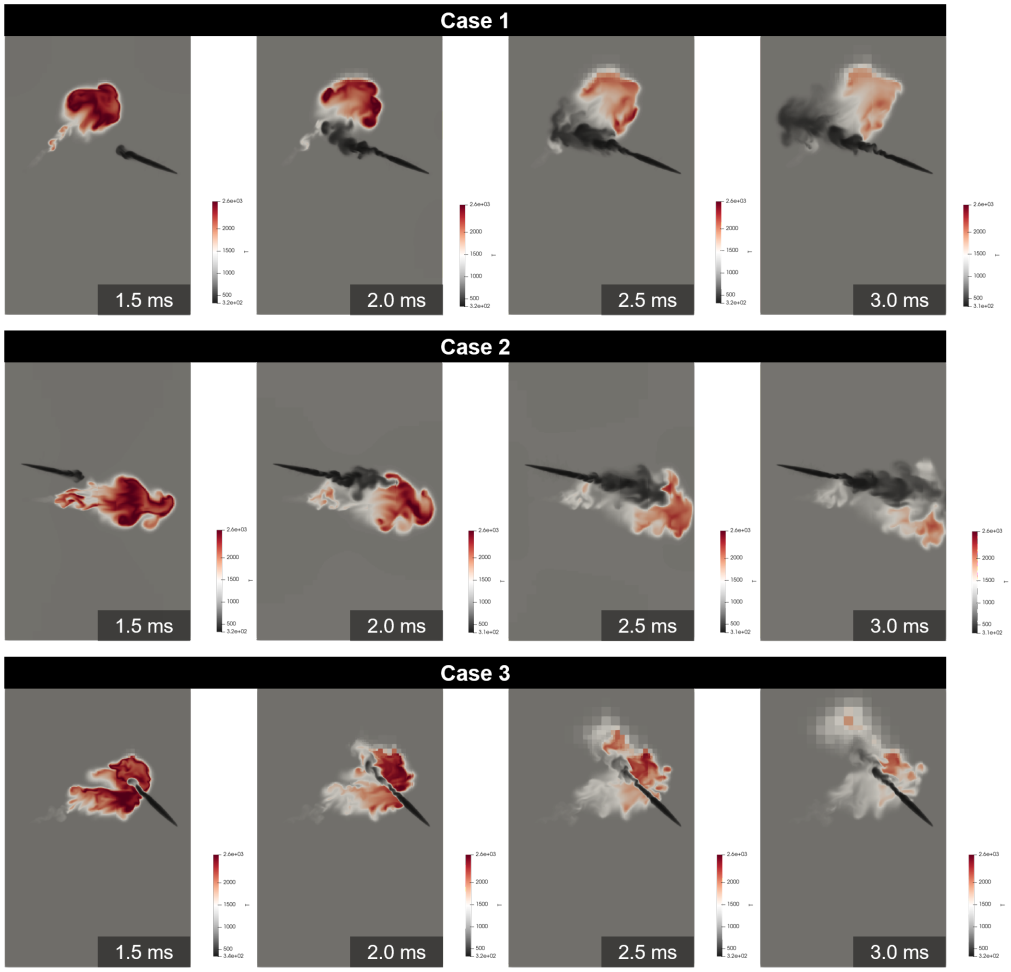

Figure 4.4: Temperature distributions of the three cases.

The transient temperature distributions of the three cases are shown in Figure 4.4. Since diesel injection started at 0 ms while ammonia injection began later at 1.2 ms, the ammonia jet will impinge on the diesel jet after the diesel jet is ignited. Based on the temperature contours, the high-temperature region can be mainly associated with the diesel combustion zone, while the relatively lower-temperature region corresponds to the ammonia jet and its surrounding mixing area. Therefore, the interaction between these two regions provides important information on the coupling between diesel ignition and ammonia combustion.

In Case 1, the diesel-induced high-temperature region remains relatively compact and is mainly located above the ammonia jet. The lower-temperature ammonia region appears to pass below or beside the main high-temperature zone, indicating that the spatial overlap between ammonia and the diesel combustion region is limited. As a result, the ammonia jet may partially miss the high-temperature core, which weakens direct

ammonia oxidation. This can explain why the high-temperature region is relatively stable and continuous, while the overall ammonia participation in the main combustion zone may be limited. Therefore, the stable temperature structure in Case 1 should not be interpreted simply as better ammonia utilization, but rather as a consequence of weak interaction between the ammonia jet and the diesel-induced high-temperature zone.

In Case 2, the high-temperature diesel region and the lower-temperature ammonia region interact more strongly along the horizontal direction. The ammonia jet appears to impinge more directly on the hot products formed by diesel combustion, resulting in a more elongated, displaced high-temperature region. However, as the lower-temperature ammonia jet continues to enter the chamber, it appears to cool and dilute part of the high-temperature zone without igniting. In summary, the temperature field in Case 2 suggests stronger local interaction between diesel combustion and ammonia injection, but also faster downstream movement and a weakening of the hot region in the later stage, without successful ammonia jet ignition before the jet reaches the wall.

In Case 3, the high-temperature and lower-temperature regions show a more complex and fragmented structure. The ammonia jet appears to interact with the diesel high-temperature region more strongly than in Case 1, but the overlap is not uniform. Instead, the hot region becomes separated into several local pockets as combustion develops. This suggests that ammonia is partly entrained into the diesel combustion zone, promoting local reactions, but the flame structure becomes less continuous in the later stage. The ammonia jet is ignited successfully, as the low-temperature region in the ammonia jet is significantly smaller than that in Cases 1 and 2.

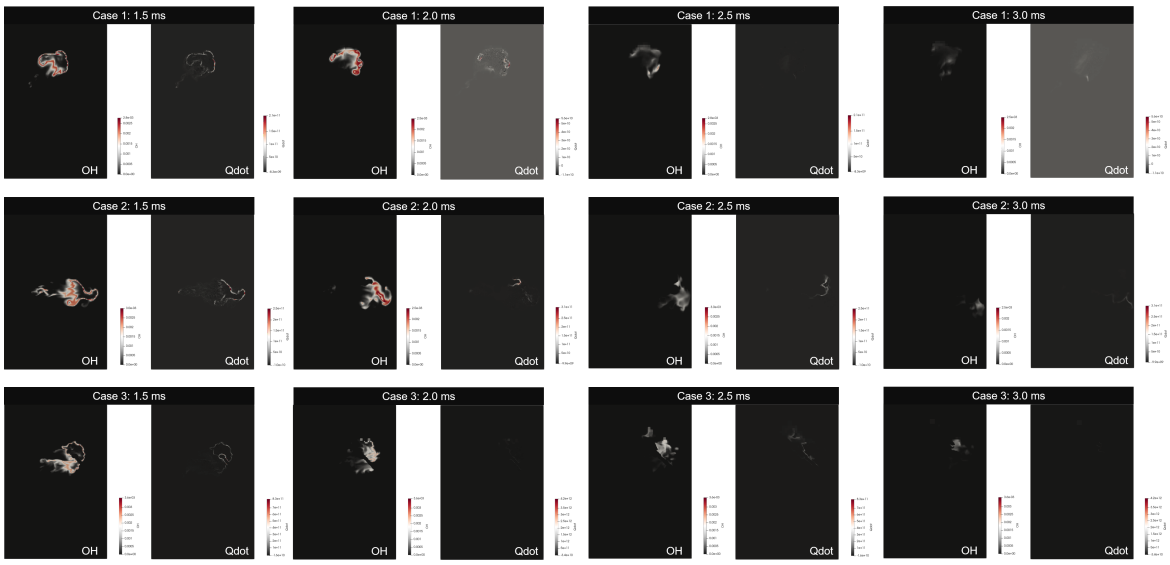

Figure 4.5: OH and Q_{dot} contours at 1.5–3.0 ms of the three cases.

The maximum OH radical and heat release rate distributions are shown in Figure 4.5. Together with the temperature contours in Figure 4.4, the OH and Qdot fields indicate that the main reaction zones are closely related to the high-temperature regions formed by diesel pilot combustion. Since ammonia is injected later, the following combustion process mainly depends on the overlap between the ammonia jet and the diesel-induced high-temperature zone.

In Case 1, the OH and Qdot regions remain localized and continuous, consistent with the compact high-temperature diesel combustion region observed in the temperature contours. However, the lower-temperature ammonia region appears to be largely separated from the main hot core. Therefore, the stable OH and Qdot distributions mainly reflect sustained reactions in diesel-induced hot products rather than strong ammonia oxidation.

In Case 2, the OH and Qdot regions are stretched along the horizontal direction, matching the elongated temperature field. This indicates more direct interaction between the ammonia jet and diesel hot products along the main spray direction, leading to concentrated local reactions and rapid heat release. The later weakening of the reaction zone suggests that the hot region is gradually diluted or quenched as the ammonia jet penetrates downstream.

In Case 3, the OH and Qdot fields become more fragmented during the later stage, consistent with the separated high-temperature regions in the temperature contours. This suggests stronger but less uniform interaction between ammonia and the diesel-induced hot region, resulting in local reaction pockets and reduced flame continuity.

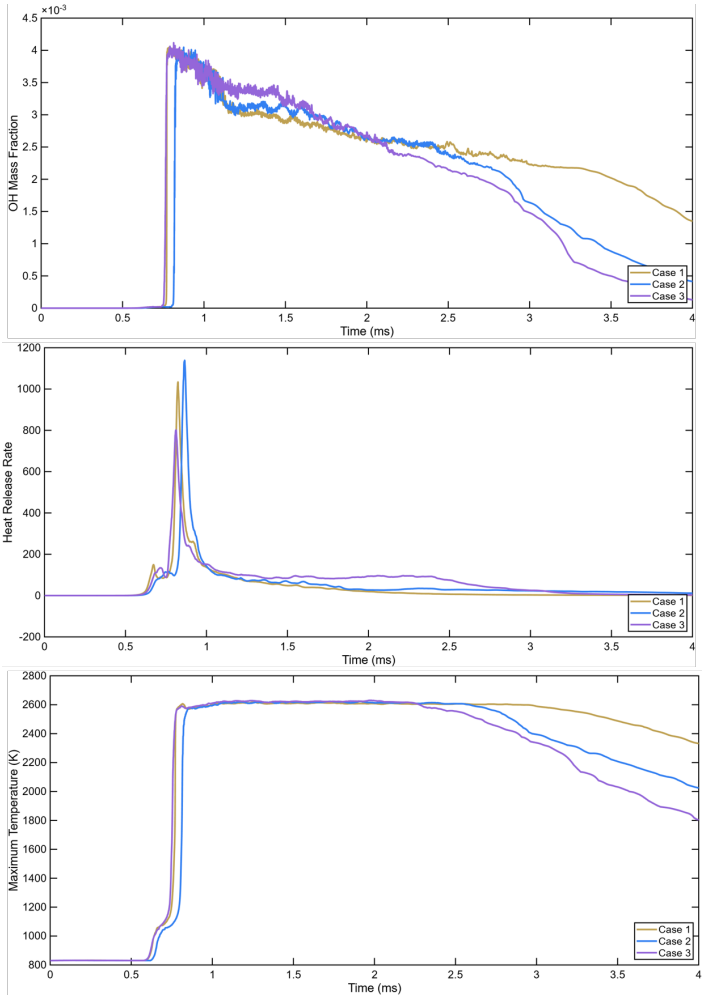

Figure 4.6: Comparisons of maximum OH mass fraction, maximum heat release rate, and maximum temperature histories in the domain of the three cases.

Figure 4.6 compares the temporal evolution of maximum OH mass fraction, maximum

heat release rate, and maximum temperature in the domain of the three cases. All cases show a rapid increase in these quantities at about 0.8 ms, owing to the auto-ignition of the diesel pilot, since ammonia is injected at 1.2 ms, after the rapid increases in OH mass fraction, heat release rate, and temperature. The heat release rate shows a low peak, followed by a high peak. The first peak is due to low-temperature ignition, which results in a minor increase in the peak temperature. The second peak is due to high-temperature ignition, associated with a rapid increase in OH mass fraction and temperature.

Case 1 maintains relatively higher OH concentration and maximum temperature during the later combustion stage, which is consistent with the compact and continuous high-temperature region observed in the temperature contours. However, this does not necessarily indicate better ammonia utilization, since the ammonia jet partially misses the main high-temperature region, as discussed earlier. The slower decay of OH and temperature may therefore mainly reflect the mixing of the diesel-induced hot products and the ambient gas. The heat release rate after 3 ms is low, indicating weak residual reactions.

Case 2 shows the highest heat release rate peak, indicating the strongest localized combustion intensity and fastest energy release. This agrees with the stretched reaction zone observed in the temperature and OH/Qdot contours. However, the later decay of OH and temperature suggests that the high-temperature reaction zone weakens after the main combustion event.

During 1 ms and 2.5 ms, Case 3 shows the highest heat release rate, indicating that the burning of ammonia is best in this case. During the later stage, e.g., after 3 ms, Case 3 shows a faster decay of OH concentration and maximum temperature. Together with the fragmented contour structures, this indicates a fast mixing of the combustion products from diesel and ammonia with the ambient gas.

Overall, the three cases show clearly different ammonia–diesel interaction mechanisms. In Case 1, the injection and transport processes of ammonia and diesel are not well synchronized. The ammonia jet tends to bypass the main high-temperature reaction zone formed by diesel combustion, resulting in weak ammonia–flame coupling. Therefore, diesel combustion appears to proceed more completely and independently, while only limited ammonia reaction occurs.

In Case 2, the ammonia jet has a strong impact on the diesel spray and its high-temperature products. At the early stage, ammonia and diesel hot products mix more directly, leading to strong localized combustion and a high heat release rate. However, as the injection continues, the ammonia jet tends to disperse the diesel-induced high-temperature region. In addition, the interaction between the mixed gases and the chamber wall further reduces the overall temperature. As a result, the reaction zone weakens rapidly during the later combustion stage, which limits the sustained oxidation of the ammonia–diesel mixture.

In Case 3, the ammonia and diesel jets collide more directly in an opposing-jet configuration. This allows ammonia to interact effectively with the high-temperature core generated by diesel combustion. Moreover, during the later stage, ammonia can still

react with the surrounding high-temperature diesel products. Unlike Case 2, where the diesel hot region is strongly dispersed by the ammonia jet, Case 3 maintains a more favorable high-temperature environment for continued ammonia oxidation, leading to better late-stage reaction persistence.

4.4 NO and N_2O emissions

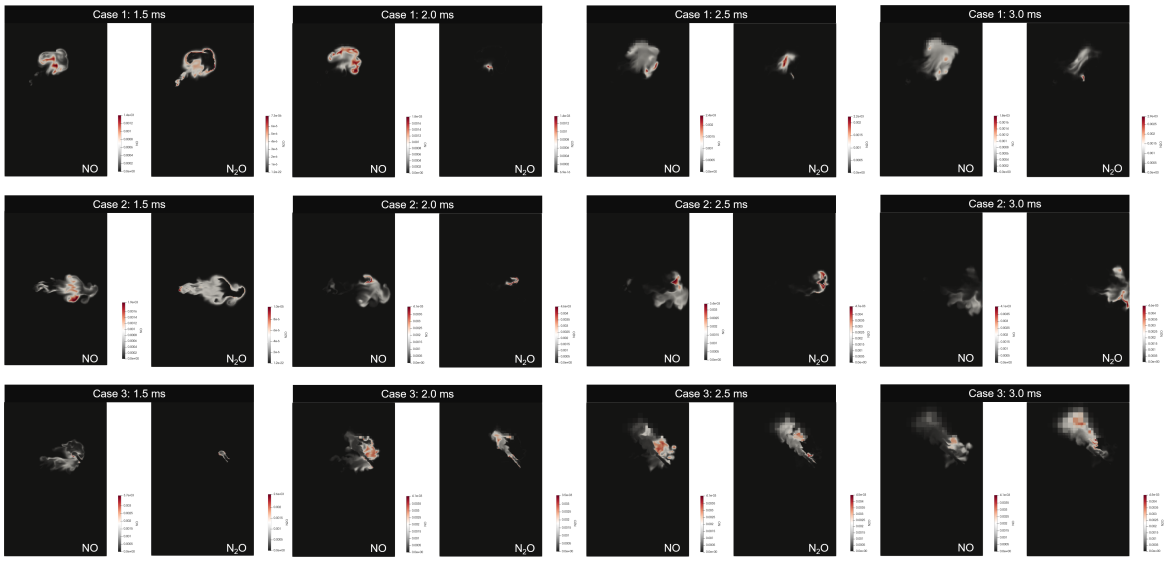

Figure 4.7: NO and N_2O contours at 1.5–3.0 ms of the three cases.

Figure 4.7 presents the spatial distributions of NO and N_2O at selected time instants for the three injection configurations. The contours show clear differences in the locations and evolution patterns of the two nitrogen-containing species. NO is mainly formed near the high-temperature reaction zones, while N_2O is more confined to the flame edges and relatively lower-temperature regions. This indicates that the formation of NO is closely related to intense high-temperature combustion, whereas N_2O is more associated with incomplete ammonia oxidation and intermediate-temperature reaction pathways.

Among the three cases, the pollutant distributions are strongly affected by the jet orientation. In Case 1, both NO and N_2O remain relatively localized, suggesting a more confined reaction zone. In Case 2, the distributions become more fragmented and dispersed, indicating that the injection angle leads to a less continuous reaction structure. In Case 3, the species distributions are stretched along the main jet direction, indicating stronger interaction between the fuel jets and a wider reaction region. Overall, the contour results demonstrate that the injection angle changes the spatial coupling between the diesel ignition region and the ammonia jet, thereby influencing the formation regions of NO and N_2O.

As shown in Figure 4.8, the domain-averaged NO mass fraction shows clear differences among the three injection cases.

In Case 1, NO increases slowly and remains at a relatively low level. This suggests

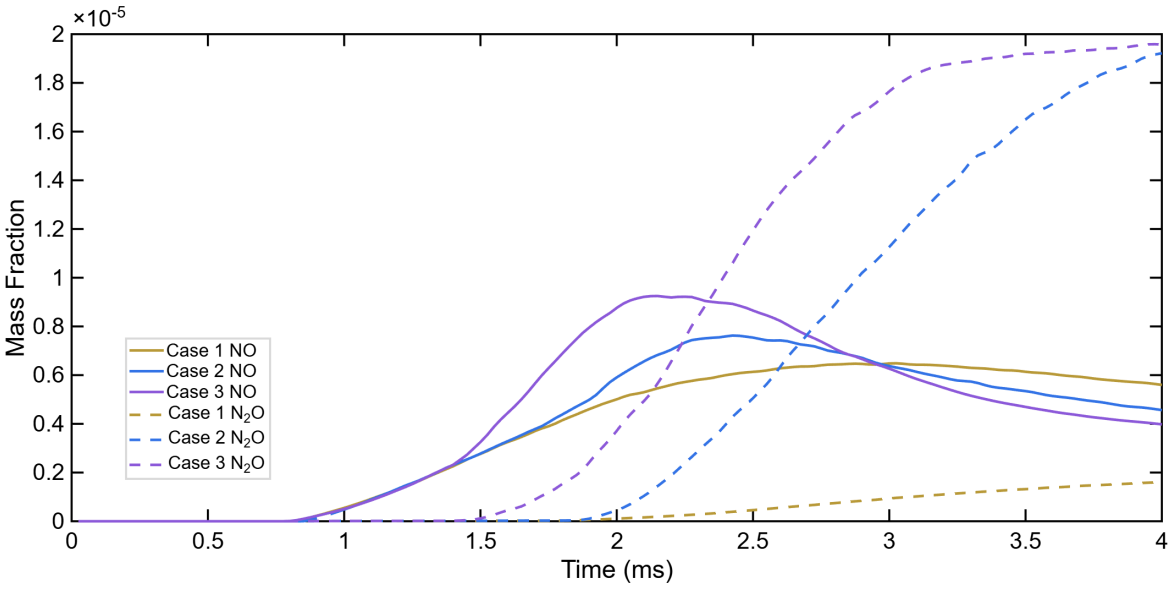

Figure 4.8: NO and N_2O volume-average mass fractions for the three injection cases.

that the overlap between the ammonia jet and the diesel flame is weak, resulting in a smaller high-temperature reaction zone, and NO is mainly due to the thermal-NO pathway in the diesel flame. The localized NO contour distribution also supports this interpretation.

In Case 2, the NO peak is lower than that of Case 3 but higher than that of Case 1, due to the contribution of the fuel-NO pathway of ammonia combustion. NO increases during the intermediate stage but decreases more clearly afterward. This suggests that although part of the ammonia jet is ignited, the flame and fuel jet gradually become less aligned in the later stage, reducing the coverage of the high-temperature region and limiting NO formation.

In Case 3, NO reaches the highest peak at approximately 2.0–2.3 ms. This indicates stronger spatial coupling between the ammonia jet and the diesel ignition region. The enhanced overlap allows ammonia to enter the high-temperature reaction zone more effectively, promoting rapid NO formation from the ammonia combustion.

The N_2O trend is consistent with that of NO. As shown in Figure 4.8, the N_2O mass fractions in Case 2 and Case 3 are clearly higher than those in Case 1 during the later stage. This indicates that more pronounced low- and intermediate-temperature ammonia oxidation regions are formed in these two cases. N_2O is more likely to accumulate in regions of ammonia combustion where the temperature is insufficient, the oxidation process is incomplete, or NH_3 is not fully consumed. Therefore, a higher N_2O level does not necessarily indicate more complete combustion. Instead, it suggests the presence of stronger incomplete-reaction zones in ammonia combustion.

Case 1 shows the lowest N_2O level throughout the process, suggesting that low- and intermediate-temperature ammonia oxidation is limited under this injection angle. However, this does not necessarily indicate the highest combustion efficiency, as residual NH_3, temperature distribution, OH, and Qdot should also be considered. Indeed, the ammonia jet remains largely unignited, leading to low N_2O emission.

In Case 2, N_2O rises later than in Case 3 but increases significantly during the later stage. This suggests that part of the ammonia jet may deviate from the high-temperature core and undergo slower oxidation in downstream lower-temperature regions, leading to increased N_2O formation.

In Case 3, N_2O increases earlier and reaches the highest level, indicating that the stronger interaction between the ammonia jet and diesel flame also creates wider intermediate-temperature regions around the main reaction zone. These regions promote incomplete ammonia oxidation and continuous N_2O accumulation.

The injection angle mainly affects the relative position and interaction between the diesel ignition region and the ammonia jet. This changes the degree of fuel–oxidizer mixing, the overlap between the ammonia jet and high-temperature reaction zones, and the residence time of nitrogen-containing species in different temperature regions. As a result, clear differences in NO and N_2O formation are observed among the three cases.

In Case 1, the coupling between the ammonia jet and the diesel-induced high-temperature region is relatively weak. The reaction zone is more confined, and both NO and N_2O remain at lower levels compared with the other cases. This suggests that the injection configuration in Case 1 is more favorable for reducing nitrogen-containing pollutant formation. However, the lower NO and N_2O levels alone do not necessarily indicate more complete ammonia combustion. Additional information, such as residual NH_3, OH distribution, temperature field, and Qdot, is still required to evaluate the combustion efficiency.

In Case 2, the ammonia jet interacts partially with the diesel flame during the early and intermediate stages, leading to moderate NO formation. However, as combustion develops, the flame and ammonia jet may become less well aligned due to the injection angle. Consequently, the high-temperature region cannot continuously cover the main ammonia jet. This explains why the NO level is lower than in Case 3, while N_2O increases noticeably during the later stage. The result suggests that part of the ammonia may undergo slower or incomplete oxidation in lower-temperature regions.

In Case 3, the injection configuration promotes stronger spatial interaction between the ammonia jet and the high-temperature region formed by diesel ignition. This produces a more intense local reaction zone and results in the highest NO peak among the three cases. However, the wider reaction region also creates intermediate-temperature zones around the main flame, where incomplete ammonia oxidation can occur. Therefore, Case 3 shows enhanced NO formation together with a significant increase in N_2O, indicating a higher risk of nitrogen-containing pollutant emissions.

Overall, the NO and N_2O formation trends are strongly affected by the local temperature field and the ammonia–diesel interaction. For NO, Case 3 shows the highest early peak because the ammonia jet directly collides with the diesel high-temperature core, promoting high-temperature ammonia oxidation. Case 2 also produces relatively high NO due to strong early mixing between ammonia and diesel hot products, but the later dispersion of the high-temperature region weakens NO formation. In Case 1, the weak overlap between ammonia and the diesel reaction zone limits NO production, resulting

in a lower and more gradual NO increase.

For N_2O, Case 1 remains at the lowest level because only limited ammonia participates in the reaction process. In contrast, Case 3 exhibits the earliest and highest N_2O formation, which may be related to the fragmented reaction structure and the presence of ammonia-containing intermediates in relatively lower-temperature regions around the high-temperature core. Case 2 shows a delayed but rapid increase in N_2O during the later stage, mainly because the ammonia jet disperses the diesel-induced high-temperature region and wall interaction further reduces the gas temperature, favoring low-temperature N_2O formation.

4.5 Combustion efficiency and ammonia emissions

Among the three cases, Case 1 maintained relatively higher OH concentration and maximum temperature during the later combustion stage, as shown in Figure 4.6. This is consistent with the compact and relatively continuous high-temperature and reaction zones observed in Figures 4.4 and 4.5. However, this behavior should not be interpreted directly as higher ammonia utilization or higher combustion efficiency. Based on the temperature contours, the ammonia jet in Case 1 may partially miss the main high-temperature region formed by diesel ignition. Therefore, the slower decay of OH concentration and temperature may mainly reflect the persistence of diesel-induced hot products and weak residual reactions, rather than strong ammonia oxidation.

Case 2 exhibited the highest heat release rate peak and the steepest temperature rise, indicating the strongest localized combustion intensity and the most rapid energy release among the three cases. This is consistent with the elongated reaction region observed in the temperature and OH/Qdot contours, where the ammonia jet interacts more directly with the diesel-induced high-temperature products along the main spray direction. However, after the main combustion event, both OH concentration and temperature decreased relatively quickly, suggesting that the high-temperature reaction region weakened rapidly during the later stage. Therefore, Case 2 shows strong local combustion intensity, but its late-stage reaction persistence is relatively limited.

Case 3 showed a more fragmented reaction structure during the later combustion stage, as observed in Figures 4.4 and 4.5. Although local interaction between the ammonia jet and the diesel-induced high-temperature region occurred, the overlap was not spatially uniform. As combustion progressed, the reaction zones became separated and less continuous, leading to faster decay of OH concentration and maximum temperature. This indicates reduced flame continuity and weaker late-stage thermal stability compared with the more compact structure observed in Case 1.

Figure 4.9 shows the averaged NH_3 mass fraction histories for the three injection cases. The averaged NH_3 mass fraction reflects the combined effects of ammonia injection, transport, mixing, and chemical consumption. Therefore, a lower NH_3 average mass fraction does not necessarily indicate a higher NH_3 reaction rate or more complete ammonia combustion, since the averaged value is also affected by the spatial distribution of the ammonia jet and its overlap with the high-temperature reaction

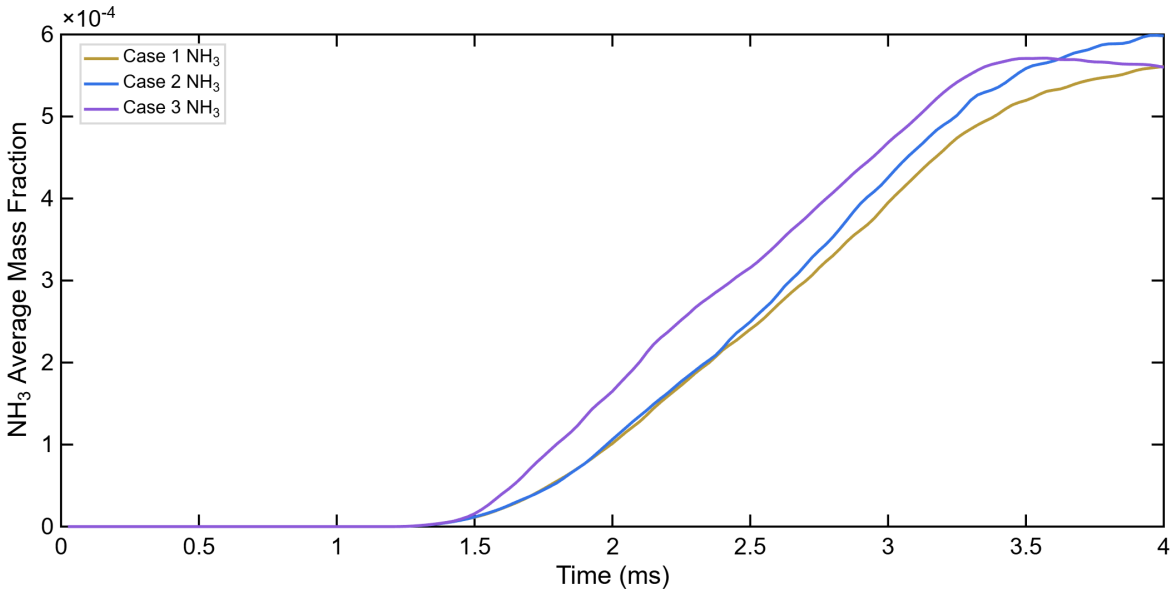

Figure 4.9: Volume-averaged NH_3 mass fraction histories for the three injection cases with the corrected case order.

region. The differences in volume-averaged NH_3 mass fraction among the three cases are relatively small because the ammonia injection mass, injection pressure, and injection duration are kept the same. In addition, the volume-averaged value represents a global quantity over the whole computational domain, which weakens the influence of local NH_3 concentration differences. Therefore, the NH_3 histories mainly reflect the overall amount of ammonia introduced into the chamber rather than the local ammonia–flame interaction. The differences among the cases are more clearly reflected in the spatial distributions of temperature, OH, Qdot, NO, and N_2O.

In Case 1, the NH_3 average mass fraction remains the lowest among the three cases. Combined with the contour results, this can be explained by the weak spatial overlap between the ammonia jet and the high-temperature region formed by diesel ignition. The ammonia jet tends to miss or deviate from the main high-temperature reaction zone, which limits ammonia oxidation. Therefore, the lower NH_3 level in Case 1 should not be interpreted simply as more complete ammonia consumption. Instead, it may indicate that the ammonia jet is more localized or does not sufficiently enter the high-temperature combustion region. This interpretation is also consistent with the relatively low NO and N_2O levels observed in this case.

In Case 2, the NH_3 average mass fraction increases continuously during the later stage and reaches the highest level near the end of the simulated period. This suggests that a considerable amount of ammonia remains in the chamber. Although part of the ammonia jet interacts with the diesel flame, the high-temperature region may not continuously cover the main ammonia jet as combustion develops. As a result, part of the NH_3 may be transported to downstream low- or intermediate-temperature regions, where oxidation is slower or incomplete. This explains the higher late-stage NH_3 level and also supports the increase in N_2O formation observed in Case 2.

In Case 3, the NH_3 average mass fraction increases earlier and remains relatively high during the intermediate stage. This indicates that the ammonia jet enters the main

flow and reaction region more effectively than in Case 1. The stronger overlap between the ammonia jet and the diesel-induced high-temperature region promotes ammonia oxidation and leads to stronger combustion activity. This is consistent with the higher NO formation in Case 3. However, the relatively high NH_3 level also suggests that not all ammonia is fully consumed, and the surrounding intermediate-temperature regions may still promote incomplete ammonia oxidation and N_2O formation.

Overall, Case 3 exhibits the earliest NH_3 increase due to stronger ammonia–diesel jet interaction, while Case 2 shows the highest late-stage NH_3 level because the high-temperature diesel region is dispersed and ammonia oxidation becomes incomplete. Case 1 maintains the lowest NH_3 level, mainly due to weak ammonia–flame coupling rather than more complete ammonia combustion.

4.6 Performance evaluation of chemistry acceleration methods

4.6.1 Computational efficiency

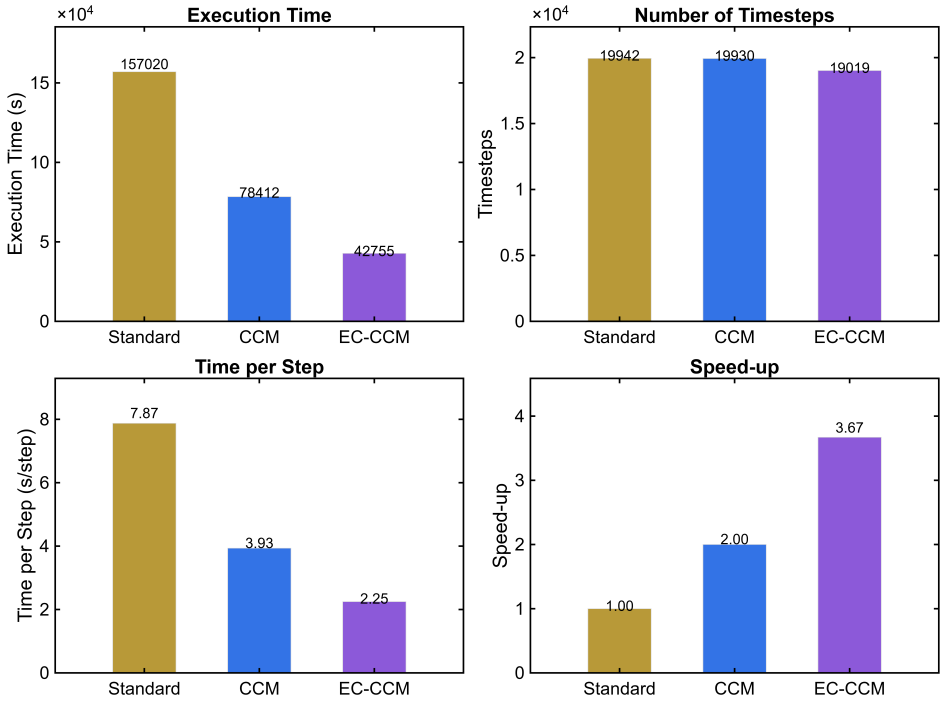

Figure 4.10: Comparison of computational time required by different chemistry acceleration methods.

The computational efficiency of the Standard, CCM, and EC-CCM methods was evaluated using the execution time and average computational cost per timestep.

As shown in Figures 4.10, the Standard solver required the longest execution time of 157020 s, while the CCM and EC-CCM methods reduced the execution time to 78411.8 s and 42754.8 s, respectively. Compared with the Standard solver, the CCM method achieved an approximately 2.0× speed-up, whereas the EC-CCM approach reached a

3.67× acceleration. The average timestep cost was also reduced from 7.87 s/step for the Standard solver to 3.93 s/step and 2.25 s/step for the CCM and EC-CCM methods, respectively.

Since all cases used the same mesh, spray configuration, and turbulence model, the reduction in timestep cost mainly resulted from the acceleration of detailed chemistry calculations.

4.6.2 Combustion prediction comparison

The combustion characteristics predicted by the Standard, CCM, and EC-CCM methods were compared using the pressure, maximum temperature, maximum OH mass fraction, and heat release histories obtained from the simulation results (as shown in Figures 4.11 and 4.12).

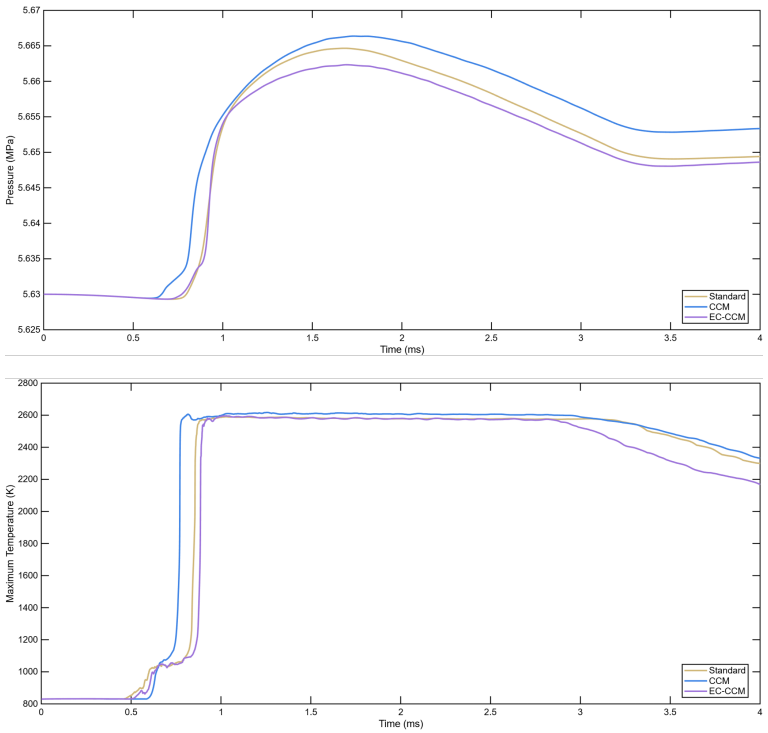

Figure 4.11: Comparison of pressure and maximum temperature histories predicted by different chemistry acceleration methods.

Table 4.2: Comparison of combustion prediction results obtained using different chemistry acceleration methods.

Case	Peak Pressure (MPa)	Peak Tmax (K)	Peak OHmax	Peak Qdot (J/ms)
Standard	5.664654	2590.162	3.971×10^{-3}	755.820
CCM	5.666369	2617.216	4.046×10^{-3}	1036.275
EC-CCM	5.662335	2596.105	3.965×10^{-3}	1413.635

For the pressure prediction, the three methods showed very similar pressure evolution trends, as shown in Figure 4.11. The peak pressures predicted by the Standard, CCM, and EC-CCM methods were 5.664654 MPa, 5.666369 MPa, and 5.662335

MPa, respectively, as listed in Table 4.2. Compared with the Standard method, the relative errors of the CCM and EC-CCM methods were approximately 0.03% and 0.04%, indicating very good agreement in pressure prediction. The chamber pressure showed the smallest difference among the three methods because it represents the overall thermodynamic response of the combustion process and is less sensitive to local reaction discrepancies.

For the maximum temperature prediction, all methods captured the rapid temperature increase after ignition and the subsequent high-temperature combustion stage. The peak temperatures predicted by the Standard, CCM, and EC-CCM methods were 2590.162 K, 2617.216 K, and 2596.105 K, respectively. Compared with the Standard solution, the EC-CCM method showed closer agreement than the original CCM method, especially during the post-ignition stage.

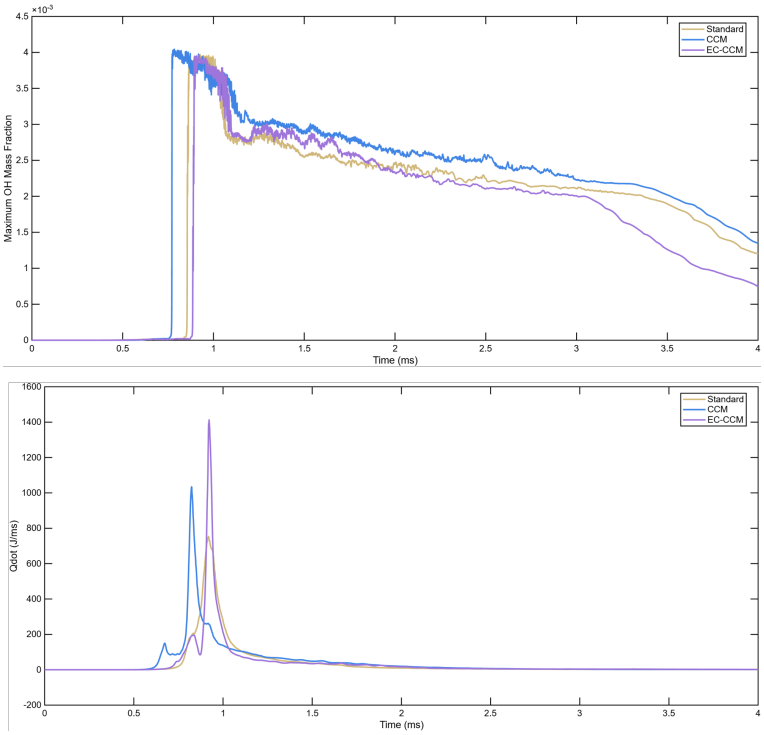

Figure 4.12: Comparison of maximum OH mass fraction and heat release rate histories predicted by different chemistry acceleration methods

The OH radical histories predicted by the three methods showed similar trends, as presented in Figure 4.12. All methods captured the rapid increase in OH formation after ignition. The peak OH mass fractions predicted by the Standard, CCM, and EC-CCM methods were 3.971×10^{-3}, 4.046×10^{-3}, and 3.965×10^{-3}, respectively, as listed in Table 4.2.

Among the three methods, the EC-CCM result showed closer agreement with the Standard solution than the original CCM method. Slight differences in ignition delay were also observed among the three methods. The CCM method predicted an earlier increase in OH formation, indicating a slightly shorter ignition delay, while the EC-CCM method showed ignition behavior closer to the Standard solution. These differences were mainly caused by the high sensitivity of the ignition process to local temperature, fuel–air mixing, and chemical reaction rates during the early combustion stage.

Compared with pressure and temperature, larger differences were observed in the heat release rate prediction. The peak heat release rates predicted by the Standard, CCM, and EC-CCM methods were 755.820 J/ms, 1036.275 J/ms, and 1413.635 J/ms, respectively, as shown in Figure 4.12 and Table 4.2.

The larger differences in heat release rate prediction were mainly caused by the high sensitivity of heat release to local reaction rates and ignition behavior during the early combustion stage. Although noticeable differences appeared near the ignition stage, all methods reproduced the overall heat release trend and combustion process.

5 Conclusions

5.1 Conclusions of the thesis

In this thesis, numerical simulations of diesel–ammonia dual-fuel combustion were carried out using OpenFOAM based on a high-pressure and high-temperature constant volume combustion chamber. The study focused on the effects of injector arrangement and fuel injection strategy on combustion characteristics, pollutant formation, and ammonia oxidation. In addition, the CCM and EC-CCM chemistry acceleration methods were evaluated to assess their applicability for detailed combustion simulations.

The simulation results show that the injection configuration has a significant influence on the interaction between the diesel-induced high-temperature region and the ammonia jet. Different injection angles changed the spatial overlap, collision behavior, and mixing process between diesel and ammonia, thereby affecting flame development, heat release, ammonia oxidation, and nitrogen-containing pollutant formation.

Among the three cases, Case 1 showed weak coupling between ammonia and the main diesel reaction zone. The injection and transport processes of ammonia and diesel were not well synchronized, so the ammonia jet tended to bypass the main high-temperature region generated by diesel combustion. As a result, diesel combustion proceeded relatively independently, while ammonia participated only weakly in the main reaction process. Therefore, the relatively low NO and N_2O levels in Case 1 should not be interpreted as better ammonia utilization, but rather as a result of limited ammonia–flame interaction.

In Case 2, the ammonia jet had a strong impact on the diesel spray and its high-temperature products. During the early stage, ammonia mixed more directly with the diesel hot products, producing the strongest localized heat release and the highest combustion intensity among the three cases. However, as the ammonia jet continued to penetrate, it dispersed the diesel-induced high-temperature region. In addition, the interaction between the mixed gases and the chamber wall further reduced the overall temperature. These effects weakened the later-stage reaction and promoted incomplete ammonia oxidation, which is consistent with the increase in NH_3 and N_2O during the later combustion stage.

In Case 3, the ammonia and diesel jets collided more directly in an opposing-jet configuration. This allowed ammonia to enter the high-temperature diesel core and react more effectively. During the later stage, ammonia could still interact with the surrounding high-temperature diesel products, resulting in more sustained ammonia oxidation compared with Case 2. This stronger high-temperature interaction promoted NO formation. Meanwhile, the fragmented reaction structure and local lower-temperature regions around the high-temperature core also contributed to earlier and higher N_2O formation.

The pollutant analysis indicates that NO formation is mainly associated with high-temperature ammonia oxidation, while N_2O is more related to relatively lower-temperature regions and incomplete ammonia oxidation. Therefore, the injection angle and injector arrangement must be carefully optimized to balance combustion intensity, ammonia utilization, NO formation, and N_2O emissions in diesel–ammonia dual-fuel combustion.

Regarding computational performance, both CCM and EC-CCM significantly reduced the computational cost compared with the Standard chemistry solver. The CCM method achieved approximately a 2.0× speed-up, while EC-CCM reached approximately 3.67×. In addition, EC-CCM showed better agreement with the Standard chemistry solution than the original CCM method in predicting pressure, temperature, and OH evolution. These results suggest that EC-CCM can effectively improve computational efficiency while maintaining acceptable prediction accuracy for detailed diesel–ammonia combustion simulations.

5.2 Future work

Future work can be divided into two main aspects: optimization of the present numerical setup and completion of the remaining research tasks.

For the optimization part, the mesh quality used in the present study was reduced in order to control the computational cost and simulation time. Although the current mesh configuration was able to capture the major combustion characteristics, some local combustion structures and detailed reaction processes may not have been predicted with sufficient accuracy. Therefore, higher-quality and finer mesh simulations will be conducted in future work to further improve the accuracy and reliability of the numerical results.

In addition, the design of the mesh refinement regions was not entirely optimal. Due to the different injection angles, fuel sprays with larger inclination angles may move outside the predefined refinement regions during the combustion process. Therefore, the refinement regions should be appropriately enlarged to ensure accurate capture of spray development and combustion phenomena throughout the entire simulation period.

For future research, the fuel for combustion could be extended from ammonia to methanol in simulations. The combustion characteristics of different fuels could be compared under similar operating conditions in order to investigate the influence of fuel properties on dual-fuel combustion behavior. The results are expected to provide further support for the development and optimization of marine engine combustion technologies.

Bibliography

[1] H. Ritchie. *Sector by Sector: Where Do Global Greenhouse Gas Emissions Come From?* Accessed: 2023-10-27. 2020. URL: https://ourworldindata.org/ghg-emissions-by-sector.

[2] F. Cheng. *Chemical Composition and Properties of Petroleum.* Accessed: 2025-11-16. 2022. URL: https://www.globalscienceresearchjournals.org/articles/chemical-composition-and-properties-of-petroleum-91039.html.

[3] Eurostat. *Final Energy Consumption in Transport - Detailed Statistics.* Accessed: 2026-05-28. 2025. URL: https://ec.europa.eu/eurostat/statistics-explained/.

[4] International Maritime Organization. *2023 IMO Strategy on Reduction of GHG Emissions from Ships.* Accessed: 2026-05-28. 2023. URL: https://www.imo.org/en/OurWork/Environment/Pages/2023-IMO-Strategy-on-Reduction-of-GHG-Emissions-from-Ships.aspx.

[5] Everllence. *Engines for Future Fuels.* Accessed: 2026-05-25. 2025. URL: https://www.everllence.com/our-focus/future-technologies/future-fuels-engines.

[6] Boris Stolz, Maximilian Held, Gil Georges and Konstantinos Boulouchos. "Techno-Economic Analysis of Renewable Fuels for Ships Carrying Bulk Cargo in Europe". In: *Nature Energy* 7.3 (2022), pp. 203–212. DOI: 10.1038/s41560-021-00957-2.

[7] Fayas Malik Kanchiralla, Selma Brynolf, Tobias Olsson, Joanne Ellis, Julia Hansson and Maria Grahn. "How Do Variations in Ship Operation Impact the Techno-Economic Feasibility and Environmental Performance of Fossil-Free Fuels? A Life Cycle Study". In: *Applied Energy* 350 (2023), p. 121773. DOI: 10.1016/j.apenergy.2023.121773.

[8] Xinyi Zhou, Tie Li, Run Chen, Yijie Wei, Xinran Wang, Ning Wang, Shiyan Li, Min Kuang and Wenming Yang. "Ammonia Marine Engine Design for Enhanced Efficiency and Reduced Greenhouse Gas Emissions". In: *Nature Communications* 15 (2024), p. 2110. DOI: 10.1038/s41467-024-46366-2.

[9] Leilei Xu, Shijie Xu, Xue-Song Bai, Juho Aleksi Repo, Saana Hautala and Jari Hyvönen. "Performance and Emission Characteristics of an Ammonia/Diesel Dual-Fuel Marine Engine". In: *Renewable and Sustainable Energy Reviews* 185 (2023), p. 113631. DOI: 10.1016/j.rser.2023.113631.

[10] Amin Yousefi, Hongsheng Guo, Shouvik Dev, Brian Liko and Simon Lafrance. "Effects of Ammonia Energy Fraction and Diesel Injection Timing on Combustion and Emissions of an Ammonia/Diesel Dual-Fuel Engine". In: *Fuel* 314 (2022), p. 122723. DOI: 10.1016/j.fuel.2021.122723.

[11] Yuchen Zhou, Shijie Xu, Leilei Xu and Xue-Song Bai. "Ignition, combustion modes and NO/N2O emissions in ammonia/n-heptane combustion under RCCI engine conditions". In: *Combustion and Flame* 280 (2025), p. 114352.

[12] Karl Oskar Pires Bjørgen, David Robert Emberson and Terese Løvås. "Combustion of Liquid Ammonia and Diesel in a Compression Ignition Engine Operated in High-Pressure Dual Fuel Mode". In: *Fuel* 360 (2024), p. 130269. DOI: 10.1016/j.fuel.2023.130269.

[13] Leilei Xu, Pengbo Dong, Zhenxian Zhang, Jingqi Bu, Jiangping Tian, Wuqiang Long, Haifeng Liu and Xue-Song Bai. "Impact of Spray Interaction on Ammonia/Diesel Dual-Fuel Combustion and Emission under Engine Relevant Conditions". In: *Proceedings of the Combustion Institute* 40.1–4 (2024), p. 105751. DOI: 10.1016/j.proci.2024.105751.

[14] Leilei Xu, Margherita Miccio, Pengbo Dong, Zhenxian Zhang, Wuqiang Long and Xue-Song Bai. "Combustion and emission characteristics in a two-stroke direct-injection compression-ignition ammonia/diesel dual-fuel engine". In: *Fuel* 422 (2026), p. 139142. DOI: 10.1016/j.fuel.2026.139142.

[15] Xianghe Chu, Jialin He, Lining Feng, Linxun Xu, Xiongbo Duan and Zhiqiang Sun. "Effects of Ammonia Energy Ratio and Hydrogen Addition on the Performance of Ammonia-Diesel Dual-Fuel Engine". In: *Energy* 335 (2025), p. 138206. DOI: 10.1016/j.energy.2025.138206.

[16] Yuchen Zhou. "Detailed Numerical Simulation of Ammonia/Diesel Combustion under CI Engine Conditions". PhD Thesis. Lund, Sweden: Lund University, 2025.

[17] Mehdi Jangi, Rixin Yu and Xue-Song Bai. "Development of Chemistry Coordinate Mapping Approach for Turbulent Partially Premixed Combustion". In: *Flow, Turbulence and Combustion* 90.2 (2013), pp. 285–299. DOI: 10.1007/s10494-012-9412-1.

[18] Yuchen Zhou, Shijie Xu, Leilei Xu and Xue-Song Bai. "An error-controlled chemistry coordinate mapping approach for numerical simulation of turbulent combustion". In: *Proc. Combust. Inst., accepted for publication* (2026).

[19] H. Jasak, A. Jemcov and Z. Tukovic. "OpenFOAM: A C++ Library for Complex Physics Simulations". In: *International Workshop on Coupled Methods in Numerical Dynamics*. Vol. 1000. IUC Dubrovnik, Croatia, 2007.

[20] Leilei Xu, Shijie Xu, Xingcai Lu, Ming Jia and Xue-Song Bai. "Large Eddy Simulation of Spray and Combustion Characteristics of Biodiesel and Biodiesel/Butanol Blend Fuels in Internal Combustion Engines". In: *Fuel* 280 (2020), p. 118530. DOI: 10.1016/j.fuel.2020.118530.

[21] Pierre Sagaut. *Large Eddy Simulation for Incompressible Flows*. Springer, 2006.

[22] Leilei Xu, Yachao Chang, Mark Treacy, Yuchen Zhou, Ming Jia and Xue-Song Bai. "A skeletal chemical kinetic mechanism for ammonia/n-heptane combustion". In: *Fuel* 331 (2023), p. 125830.

[23] Leilei Xu, Xue-Song Bai, Ming Jia, Yong Qian, Xinqi Qiao and Xingcai Lu. "Experimental and Modeling Study of Liquid Fuel Injection and Combustion in Diesel Engines with a Common Rail Injection System". In: *Applied Energy* 230 (2018), pp. 287–304. DOI: 10.1016/j.apenergy.2018.08.104.

[24] Pierre Vauquelin, Yuchen Zhou, Arvid Å kerblom, Christer Fureby and Xue-Song Bai. "Chemistry Mapping in Large-Eddy Simulations of Bluff-Body Flames Using Alternative Jet Fuels". In: *AIAA Journal* (2024). DOI: 10.2514/1.J065789.

[25] Zhenxian Zhang, Wuqiang Long, Zechuan Cui, Pengbo Dong, Jiangping Tian, Hua Tian and Xiangyu Meng. "Visualization study on the ignition and diffusion combustion process of liquid phase ammonia spray ignited by diesel jet in a constant volume vessel". In: *Energy Conversion and Management* 299 (2024), p. 117889.